Far Infrared Reflectance Along the C-axis of the Charge Stripe Superconductor $La_{1.875}Ba_{0.125}CuO_4$

by

Brad Dempsie

A THESIS SUBMITTED IN PARTIAL FULFILMENT OF
THE REQUIREMENTS FOR THE DEGREE OF

MASTER OF SCIENCE

in

The Faculty of Mathematics and Sciences

Department of Physics

BROCK UNIVERSITY

July 31, 2010

In presenting this thesis in partial fulfilment of the requirements for an advanced degree at the Brock University, I agree that the Library shall make it freely available for reference and study. I further agree that permission for extensive copying of this thesis for scholarly purposes may be granted by the head of my department or by his or her representatives. It is understood that copying or publication of this thesis for financial gain shall not be allowed without my written permission.

(Signature) Brad Dempsee

Department of Physics

Brock University
St.Catharines, Canada

Date August 19/2010

Abstract

Reflectance measurements along the c-axis of $La_{1.875}Ba_{0.125}CuO_4$ at temperatures above(6K) and below(0.5K) the bulk superconducting transition temperature(3K) were performed using a Bruker rapid scan spectrometer and a Martin-Puplett polarizing spectrometer. It was found that when polarized light reflected from a sample the Bruker rapid scan spectrometer has a low frequency cutoff of $10cm^{-1}$ while the Martin-Puplett polarizing spectrometer has a low frequency cutoff of $6cm^{-1}$. A superconducting plasma edge was absent in all measurements taken. It was concluded that if a superconducting plasma edge exists in $La_{1.875}Ba_{0.125}CuO_4$, it is below $6cm^{-1}$.

Contents

List of Figures

List of Tables

Acknowledgements

I would like to thank Dr. Maureen Reedyk first and foremost for accepting me as a graduate student and for her guidance and support throughout my graduate degree. I would also like to thank Chris Homes for providing a sample and high frequency reflectivity measurements and Dr. Razavi for the use of his MPMS system for magnetic susceptibility measurements. A special thanks to Dr. Crandles for advice and help in the lab. I would also like to thank Mike Potalivo, Patrick Reuvenkamp and Mojtaba Hajialamdari for helping me with my project. Furthermore I want to thank the entire Physics Department at Brock University for providing an amazing two years of graduate education.

Chapter 1

Introduction

The family of high temperature superconductors (also called cuprates) possess some of the highest known superconducting transition temperatures. The electronic transport properties that lead to this superconductivity are not yet fully understood. Copper oxide layers are believed to be responsible for superconductivity occurring within the a-b planes which they occupy. The c-axis electron transport properties are not so well understood.

Spin density waves (SDW's) occur as a periodic ordering of spins on a crystal lattice. These spins may also occur in a static "stripe" form where the spins on individual atoms remain constant throughout time. The spins occur in alternating patterns forming ferromagnetic and anti-ferromagnetic regions along the crystal lattice. Charge density waves occur when the crystal lattice re-orders itself to allow conduction electrons to propagate through the lattice in "waves". Electrons may also propagate through the lattice along a specific periodic path in the unit cell. This is a "static" charge density wave or a charge stripe. Charge and spin stripe ordering have been measured in doped samples of $La_{2-x}Ba_xCuO_4$ when x=1/8 [1] [2]. The charge and spin stripe order appear to be related indirectly to the superconductivity of the cuprates. The bulk superconductivity is reduced from 30K in optimally doped $La_{2-x}Ba_xCuO_4$ to 2.4K in $La_{1.875}Ba_{0.125}CuO_4$. The stripes appear to compete with the superconducting state. The onset of the Tc occurs at a much higher value as can be seen in Figure 1.1. This suggests that there may be two separate mechanisms

involved in the superconducting state. [2] The superconductivity in the Cu-O plane or along the a and b directions may be caused by a different mechanism than along the c-axis.

The plasma edge (or plasma frequency) is the characteristic frequency at which the free electron gas (or plasma) oscillates in a metallic sample. The goal of this thesis work was to search for a plasma edge in $La_{1.875}Ba_{0.125}CuO_4$ along the c-axis of a single crystal sample in the superconducting state. Knowledge of the low frequency reflectance will allow an accurate determination of the optical conductivity along the c-axis which may lead to a better picture of the electronic structure of $La_{1.875}Ba_{0.125}CuO_4$. This could provide insight into the different superconducting mechanisms that occur along the c-axis and the a-b plane in $La_{1.875}Ba_{0.125}CuO_4$ and other cuprates.

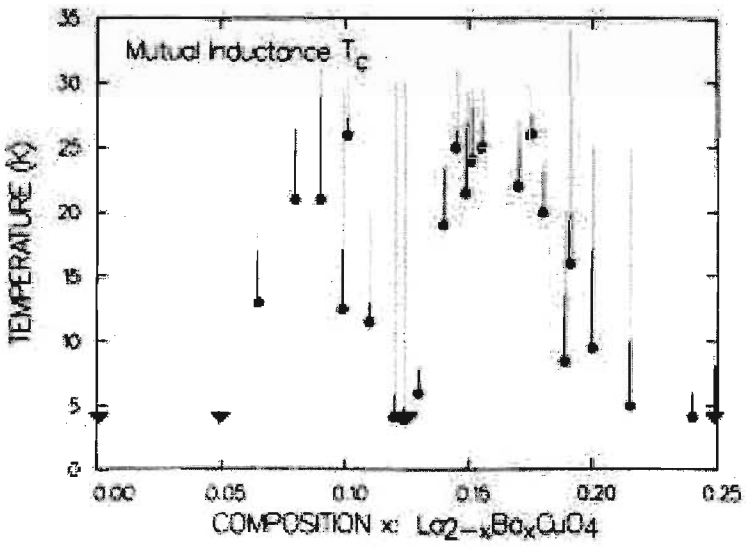

Figure 1.1: The superconducting transition temperature of $La_{2-x}Ba_xCuO_4$ for different values of x. Dotted lines represent the highest onset and solid lines represent the bulk onset of Tc. [3]

$La_{1.875}Ba_{0.125}CuO_4$ exhibits typical metallic behavior in the a-b plane. As temperature is decreased the resistivity decreases. The a-b plane acts as a conductor, with a plasma edge that onsets at about 1 eV or about 8000cm^{-1}. The c-axis acts as an insulator until the onset of bulk superconductivity. The lack of a plasma edge above 50cm^{-1} suggests that there is either a very small superconducting electron density or a new mechanism for superconductivity along the c-axis.

1.1 Crystal Structure

$La_{2-x}Ba_xCuO_4$ exhibits a tetragonal lattice at high temperatures (above 200K). This is referred to as the high temperature tetragonal or HTT phase. The unit cell is shown in Figure 1.2.

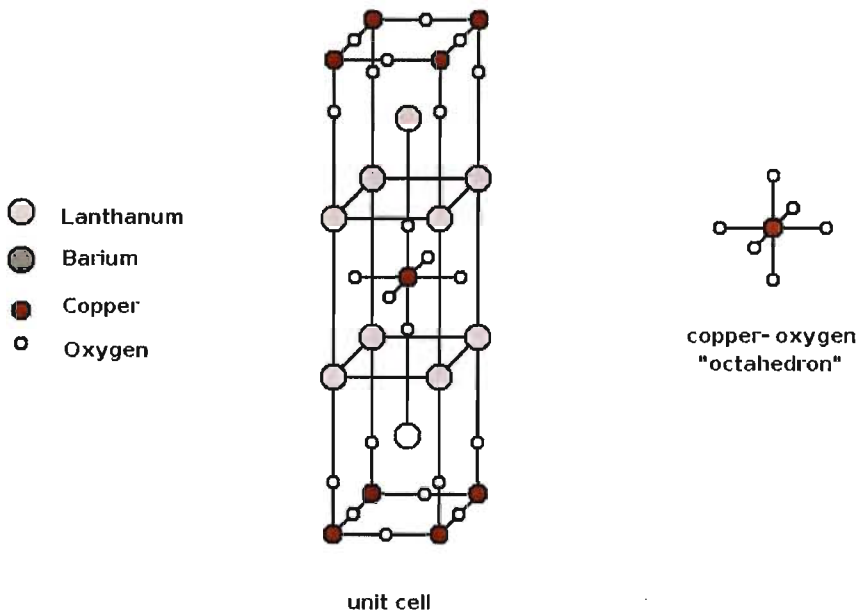

Figure 1.2: The Unit Cell of the tetragonal perovskite $La_{2-x}Ba_xCuO_4$. The copper atom in the middle of the unit cell is the corner for other identical cells.

The central "layer" of the unit cell can be recognized as a perovskite. The central

Cu atom in the unit cell will also be at the corner of another identical unit cell. $La_{2-x}Ba_xCuO_4$ can be viewed as a relative to the perovskite family, with the layers in the a-b plane following the traditional definition of the perovskite structure. Any La, Ba, or Cu atom in the corner of a perovskite "cell" is also the central atom of another cell, forming a repeating and alternating pattern along the c-axis. There is also a "space" along the c-axis between these alternating layers. This is illustrated in Figure 1.3 under the perovskite picture.

One can also view the crystal structure as the superposition of two "building block" lattices. The lattices intersect such that the corner Cu atom in lattice 1 will be directly in the middle of a unit cell in lattice 2, and vice versa. This is illustrated in Figure 1.3 under the superlattice picture.

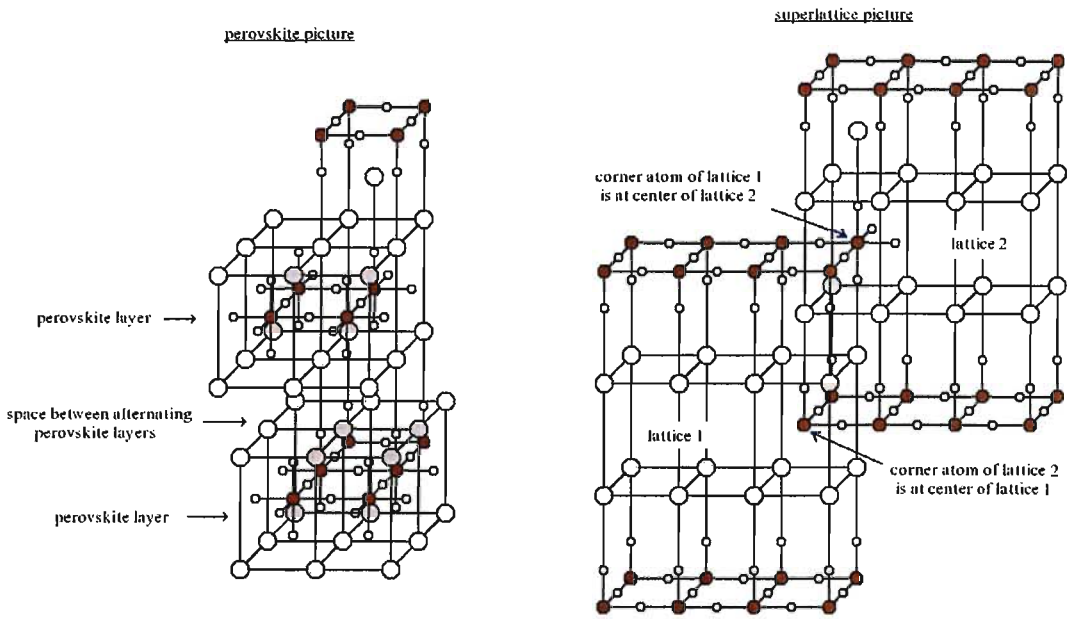

Figure 1.3: The $La_{2-x}Ba_xCuO_4$ structure is made up of 2 interpenetrating lattices which give rise to the perovskite structure.

Alternatively, the crystal structure can be viewed as "planes" of Cu-O and La/Ba-

O. This picture is illustrated in Figure 1.4. In the HTT phase the Cu-O planes are exactly aligned with the a-b plane, but the La/Ba-O "planes" are 3 dimensional. [4]

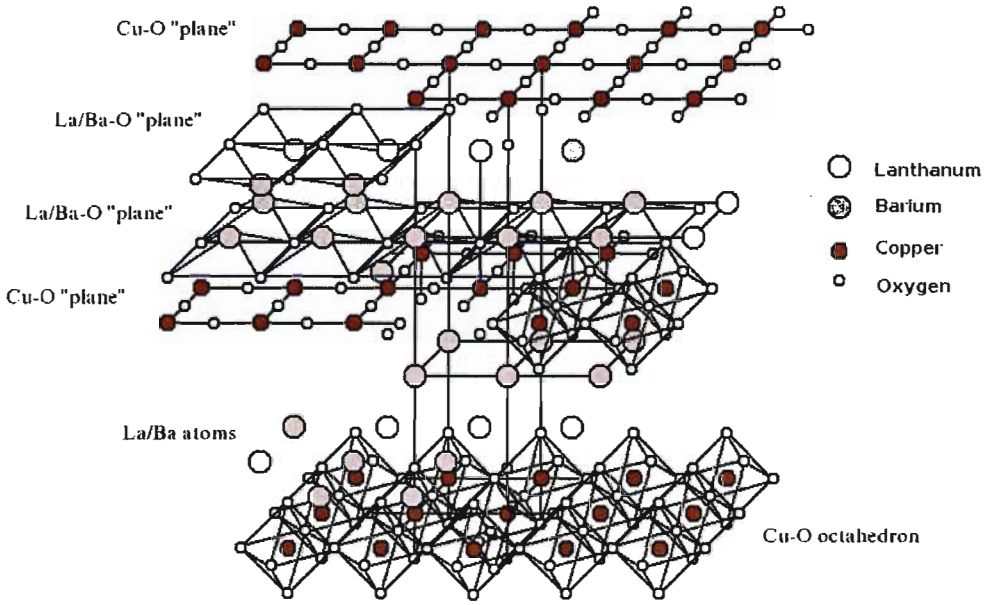

Figure 1.4: The crystal structure can be viewed as "planes" of Cu-O and La/Ba-O or as Cu-O octahedron with La/Ba planes.

$La_{2-x}Ba_xCuO_4$ enters an orthorhombic phase around 200K. [2] The Cu-O bonds along the a-b plane will no longer be at a perpendicular angle. There is a slight deviation from 90° which causes the "square" lattice along the a-b plane to appear rectangular. The Cu-O octahedra 'tilt' and the Cu-O plane buckles in response to this shift in lattice parameter. This buckling effect is shown in Figure 1.5. $La_{2-x}Ba_xCuO_4$ remains in this low temperature orthorhombic(LTO) phase until the temperature is decreased to 55K. [2] The crystal shifts to tetragonal again at this low temperature

(called the LTT phase). The Cu-O plane remains buckled in the LTT phase.

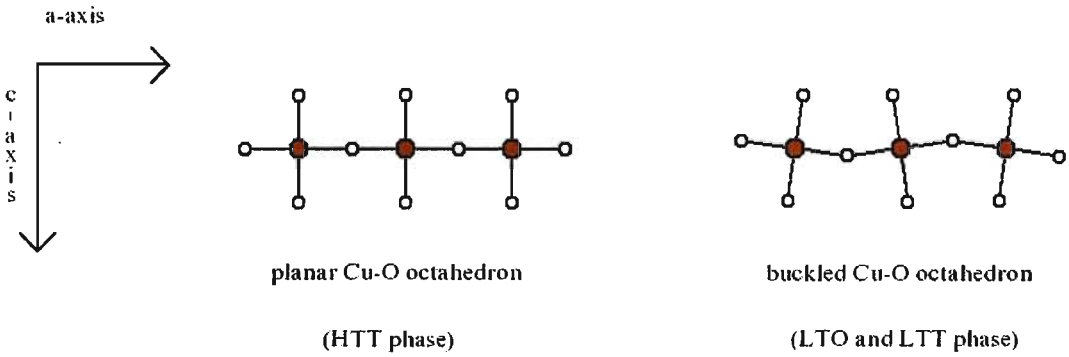

Figure 1.5: The crystal structure can be looked at as "planes" of Cu-O and La/Ba-O or as Cu-O octahedron with La/Ba planes.

1.2 Stripe Ordering

Explanations of the the electronic transport of high Tc superconductors as free electron gases have been unsuccessful. One idea that has developed to help explain the superconductivity of the cuprates is the idea of charge stripes. A stripe phase occurs when doped charges are concentrated between the domain walls of spontaneously generated antiferromagnetic insulating regions. Figure 1.6 illustrates how electrons move through these spontaneously generated regions of antiferromagnetism. Antiferromagnetic regions can be easily detected in the parent compounds of cuprates which are generally insulators. When these materials are doped they become superconducting, but the antiferromagnetic order is destroyed and instead occurs spontaneously throughout the material. These sporadically generated regions of antiferromagnetism are believed to be responsible for electron transport in the cuprates.

Tc is far below the maximum possible value for $x = 0.125$ in $La_{2-x}Ba_xCuO_4$ and periodic charge stripe ordering can be detected. [1]. For this doping, electron

movement can be observed to occur in charge stripes. The fact that charge stripes are visible in $La_{2-x}Ba_xCuO_4$ when the value of Tc is suppressed supports the idea that the stripe phase is related to the conductivity. The superconducting transition temperature increases when the stripe phase can not be detected, likely because the antiferromagnetic regions occur more sporadically. This effect may play a role in understanding how superconductivity occurs along the c-axis in the cuprates.

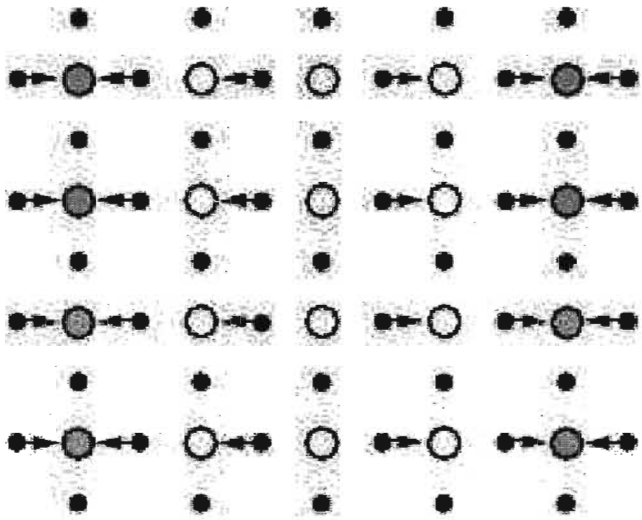

Figure 1.6: The charge stripes occurring along the a-b plane and the Cu-O phonon vibration that follows. The small dots represent the oxygen atoms and the large dots represent the copper atoms. The open circles are the high electron concentration regions while the filled in circles are hole rich. The arrows indicate the direction of phonon vibration [1]

1.3 Resistivity

Random La sites are doped with Ba, creating charge reservoirs which may either enhance or suppress the superconducting transition temperature and may change the

electronic or crystal structure of $La_{2-x}Ba_xCuO_4$. For $x = 0.125$, 1 out of every 16 random La atoms will be replaced with a Barium atom. The dependence of Tc on Barium doping is highly non-linear. Tc rises above 4K for $0.05 < x < 0.25$ with a maximum Tc occurring around 25K at $x = 0.09$ and $x = 0.15$. There is a local minimum at $x = 0.125$ where Tc once again drops below 4K (see Figure 1.1).

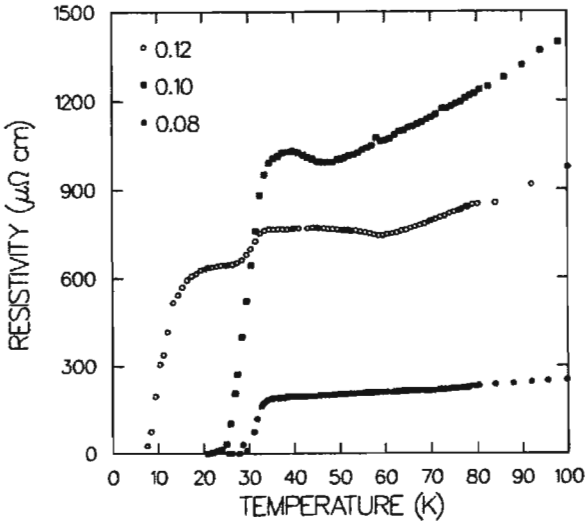

Figure 1.7: Resistivity of $La_{2-x}Ba_xCuO_4$ for different values of x. [3]

Figure 1.7 illustrates the resistivity as a function of temperature for several different Barium dopings measured within the a-b face of a polished crystal. The local minimum in resistivity for $x = 0.12$ at around 58K may be due to the LTO-LTT structural transition. The step in the resistivity that occurs between $25K$ and $35K$ and the bulk superconducting transition at 10K may be from two separate superconducting phases.

Chapter 2

Magnetic Susceptibility

2.1 Theory

Magnetic susceptibility is described as the degree to which the magnetic moments in a substance align themselves along the direction of an external magnetic field. A given sample is placed in an external magnetic field and its magnetization is measured. The magnetization is the magnetic dipole moment per unit volume. The magnetic susceptibility is therefore defined as

$$\chi = \frac{\mu M}{B} \tag{2.1}$$

where χ is the magnetic susceptibility, M is the magnetization, μ is the permeability of the medium, and B is the magnetic induction. It is easier to use this equation if it is re-written in terms of the applied magnetic field intensity, H. In materials such as ferromagnets, the response is not linear and a different formula is needed. For low response materials however Equation 2.1 can be re-written so that,

$$\chi = \frac{M}{H} \tag{2.2}$$

where χ is the magnetic susceptibility, M is the magnetization, and H is the applied field.

2.2 Characterization

2.2.1 Previous Work

Magnetic susceptibility is a simple and useful method for probing magnetic transitions that occur in a sample. Figure 2.1 shows the susceptibility curve for various samples of $La_{2-x}Ba_xCuO_4$. The bulk magnetic transitions corresponding to the superconducting state occur over a wide temperature range and are characterized by a sharp decrease in magnetization. It appears as if there is a high onset occurring before the bulk onset. For x=0.12 the deviation from unity begins at approximately 30K. The temperature does not decrease far enough to show the bulk transition.

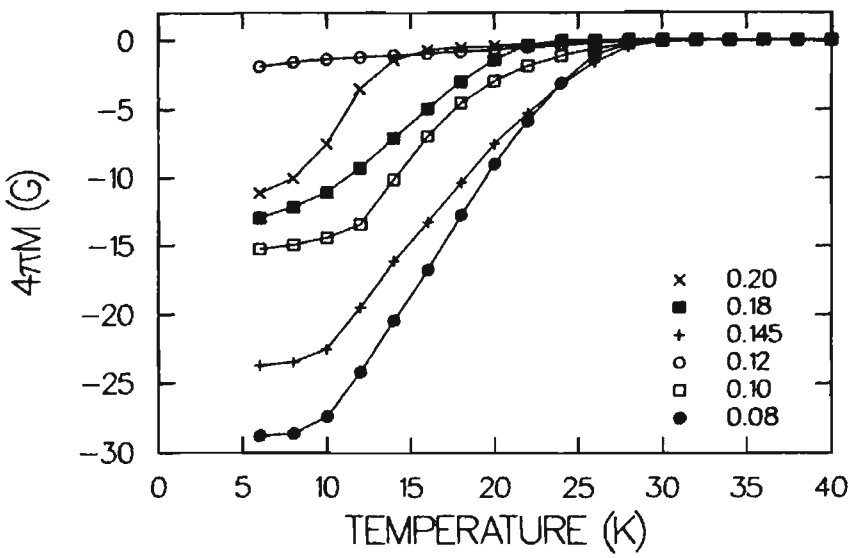

Figure 2.1: Susceptibility curves of $La_{2-x}Ba_xCuO_4$. [3]

2.2.2 Results

Magnetic Susceptibility measurements for this thesis were made using a Magnetic Property Measurement System (MPMS) equipped with a superconducting quantum

interference device (SQUID) to detect the magnetization of $La_{1.875}Ba_{0.125}CuO_4$ as a function of temperature. The results show a large transition at approximately 3K which is believed to be the bulk superconducting transition. This result is in good agreement with the transition expected from previous resistivity measurements. There is also a high onset which occurs at about 30K. This is expected from measurements made on a crystal of $La_{1.8}Ba_{0.12}CuO_4$ by Moodenbaugh et al. [3]

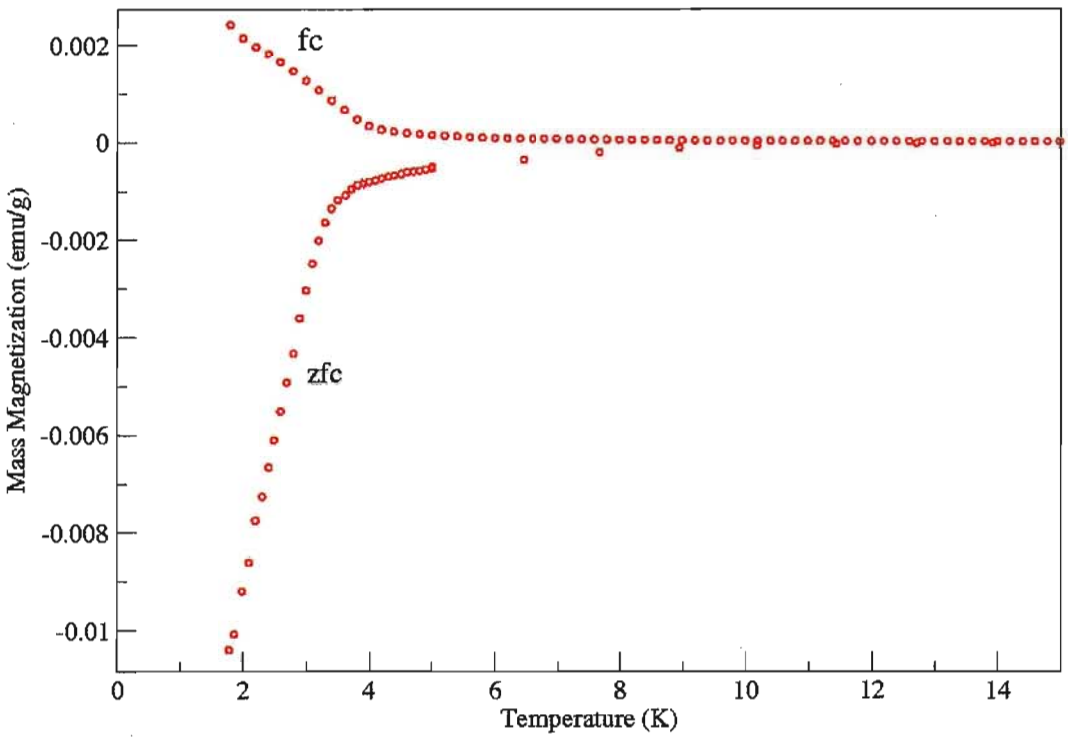

Figure 2.2: Zero field and field cooling measurements showing the bulk superconducting transition of $La_{1.875}Ba_{0.125}CuO_4$

Figure 2.2 shows the zero field cooling (ZFC) and the field cooling (FC) curves on our sample of $La_{1.875}Ba_{0.125}CuO_4$. A magnetic field of 20 Gauss with H||c was used. In the ZFC curve the sample begins below the superconducting transition temperature. A magnetic field is then applied. The magnetization on the surface

of the sample opposes the applied magnetic field. This large negative magnetization is a result of the superconductivity of the sample. Below 3K the magnetization has a large dependence on temperature. Above 3K this temperature dependence on magnetization decreases. This marks the end of bulk superconductivity in the sample. The residual magnetization which is observed as a slight dependence of magnetization on temperature below 30K is likely a result of filamentary superconductivity occurring along the a-b plane. [3]

The field cooling curve is taken with the magnetic field applied above Tc. The temperature is then decreased. The results for $La_{1.8}Ba_{0.12}CuO_4$ are characteristic of a high temperature superconductor with a paramagnetic Meissner effect(PME). In the PME spontaneous orbital currents from the superconducting current occur just as spontaneously as in the diamagnetic Meissner effect. The currents in the PME case have similar temperature dependence but occur in the opposite direction and without the need of an external field. [5].

The magnetization in the FC curve increases with decreasing temperature. The FC curve behaves similar to the ZFC curve, exhibiting a small magnetic response below 30K followed by a sharp transition. The absolute value of magnetization is smaller in the FC curve. The bulk onset in the FC curve occurs around 4K, slightly higher in temperature than in the ZFC case as expected. It is concluded that bulk superconductivity in this sample of $La_{1.875}Ba_{0.125}CuO_4$ occurs at 3K.

Chapter 3

Optical Properties

3.1 Theory

3.1.1 Low Energy Spectroscopy

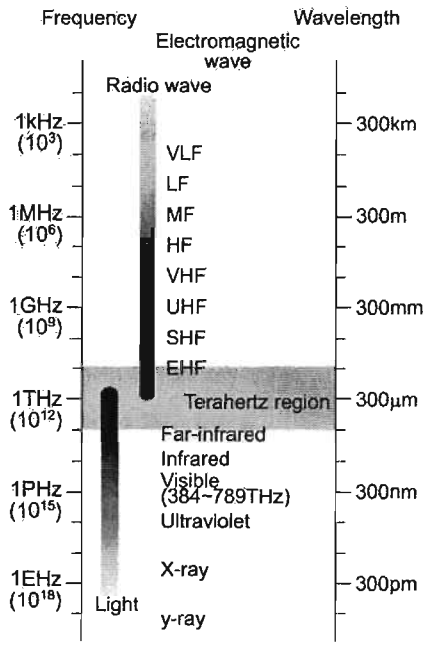

Figure 3.1: The electromagnetic spectrum around the millimeter wavelengths

A key measurement to the physicist is that of energy. How energy interacts with matter, at a given time and space is the way in which the physical world is examined. Experimenting on the atomic and sub-atomic levels of physics requires several types

of instrumentation. Varying factors such as doping concentration, temperature or pressure can be used to investigate how energy changes occur in a sample. Light gives much insight into the microscopic behavior of matter. By using light with both high and low frequency as an energy source, condensed matter systems can be probed for the movement of electrons and phonon vibrations. The electromagnetic spectrum is shown in Figure 3.1. As measurements on a sample are shifted from the region of visible and infrared radiation toward the longer microwaves, the energy which is being probed decreases. This requires more sensitive detectors and a higher signal to noise ratio. Large energies are required to remove electrons which are bound to atomic cores. X-ray radiation is used to excite electrons from bound states. Raman and infrared radiation do not contain enough energy to excite a bound electron but can instead excite phonon vibrations in a crystal. Raman spectroscopy can also be used to detect plasmons. Plasmons are quantized excitations of the free electron gas (or plasma).

3.1.2 Infrared Absorption

Photons of infrared light have less energy than the x-ray radiation that excites bound electrons from the ground state. Infrared radiation will characteristically be absorbed by the covalent bonds between atoms in a solid. The bonds themselves act like springs which can oscillate and rotate in several unique ways. When light containing the same frequency of oscillation is incident on a sample, it can be transmitted as a polariton, which is an electromagnetic wave propagation through the solid as a phonon. Free electrons oscillate in a solid at a given frequency known as the plasma frequency. The oscillating free electrons produce an electric field. Infrared radiation that has less energy than the electric field tends to be reflected from the sample.

3.1.3 Plasma Frequency

Consider a region of electric charge from the free electrons in a metal that has been uniformly translated a distance of δx. This will leave a region of net positive charge of the same size. These unbalanced regions will have an electric force of attraction. In the absence of a damping force the free electrons will overshoot the positive region and continue to oscillate in this manner at a characteristic frequency known as the plasma frequency. [6]

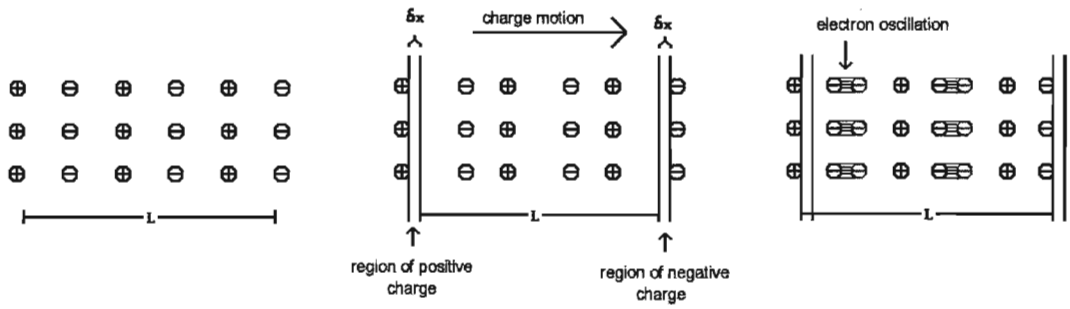

Figure 3.2: plasma oscillations

The charge on either side will be $enA\delta$x where A is the cross sectional area of the region and n is the electron density. A uniform electric field $E = \frac{en}{\epsilon_0}\delta x$ develops between the regions. If V is the total volume of the system then the force on all the electrons will be given by

$$F = qE = -enVE = -\frac{1}{\epsilon_0}n^2e^2V\delta x. \tag{3.1}$$

A negative sign is required because the force produced by the electric field of the atomic cores is acting on negatively charged electrons. Newton's second law can then be applied

$$F = ma = mnV\frac{d^2\delta x}{dt^2} = -\frac{1}{\epsilon_0}n^2e^2V\delta x. \tag{3.2}$$

The acceleration can then be found

$$\frac{d^2\delta x}{dt^2} = \frac{-\frac{1}{\epsilon_0}ne^2\delta x}{m}. \tag{3.3}$$

The solution to this differential equation is an undamped harmonic oscillator and is given by

$$\delta x(t) = sin\sqrt{\frac{\frac{1}{\epsilon_0}ne^2}{m}}t. \tag{3.4}$$

So the frequency of the oscillations, known as the plasma frequency w_p is given by

$$w_p^2 = \frac{ne^2}{\epsilon_0 m}. \tag{3.5}$$

The electric field of the light that lies below the plasma frequency will be screened by the electric field of the charge carrying electrons. Equation 3.5 indicates that the higher the density of electrons in a sample, the higher the frequency and therefore energy of the plasma.

This will cause only higher energy light to be transmitted through the sample. Almost all light below the plasma frequency will be reflected. Light which is higher in frequency than the plasma will contain too much energy to be screened out by the electric field produced by the oscillating electrons.

The optical phenomena in which the reflectance peaks sharply to unity around the plasma frequency is called the plasma edge. Refer to Appendix A for a detailed derivation of the reflectance of a metal.

Ordinary metals can be viewed as a gas of noninteracting mobile electrons. Due to the large number of free electrons in metals the plasma frequency will be high. A normal metal will have a plasma frequency around 10000cm^{-1} The High Tc cuprates exhibit an unconventional metallic response in the a-b plane with a plasma like edge near 8000cm^{-1}. The c-axis in the cuprates behaves like an insulator in the normal state and no plasma edge is visible. Below the superconducting transition electron transport begins to occur along the c-axis. A plasma edge appears at very low frequencies often on the order of 100cm^{-1}.

The plasma edge in $La_{1.875}Ba_{0.125}CuO_4$ lies at an energy of about 1eV in the a-b plane. The carrier density increases with decreasing temperature until the charge stripe order sets in. [7] The charge density along the c-axis is much lower than in the a-b plane. Once the onset of superconductivity in the bulk of $La_{1.875}Ba_{0.125}CuO_4$ occurs, free electrons should conduct in all directions through the crystal. A plasma edge should be visible in the now conducting, and hence metallic c-axis. Previous measurements done by C. Homes above 20cm^{-1} (presented in Figure 3.4) have not found a plasma edge along the c-axis in $La_{1.875}Ba_{0.125}CuO_4$ and so it is expected to occur below 50cm^{-1}. Electrons must conduct along the c-axis in order for bulk superconductivity to exist, but how many, if any, electrons exist in this state? It is important to probe as low in frequency as possible to reveal the c-axis transport. The energy of the plasma edge in the c-direction of $La_{1.875}Ba_{0.125}CuO_4$ may point towards the mechanism for its superconductivity.

3.1.4 Kramers-Kronig Relation

The following is based on the Kramers-Kronig derivation given in Optical Properties of Solids [8] and Optical Probes of Electron Correlations in Solids [9]. The principle of causality, that no effect can precede its cause is the basis for Kramers-Kronig analysis.

The induced current, $J(t)$, due to an electric field, $E(t)$, is related to the memory function, $M(t-t')$ according to

$$J(t) = \int_{-\infty}^{t} M(t-t')E(t')dt'. \tag{3.6}$$

This memory function has the property that for $t<t'$, $M(t-t') = 0$. When a driving force is applied at time $t = t'$ a current will exist. The fourier transform of M is

$$\hat{\sigma}(\omega) = \int_{0}^{\infty} M(\tau)e^{i\omega\tau}d\tau'. \tag{3.7}$$

The integral can then be split into the real and imaginary parts using the transformation $\omega \rightarrow z = \omega_1 + i\omega_2$

$$\hat{\sigma}(\omega) = \int_{0}^{\infty} M(\tau)e^{i\omega_1\tau}e^{-\omega_2\tau}d\tau'. \tag{3.8}$$

The second exponent in the integral is bounded in the upper half plane when $\tau > 0$ and in the lower half plane when $\tau<0$. The integral in the upper half plane can be evaluated since M = 0 for $\tau<0$. Since all poles occur on the real axis, the complete contour is zero

$$\oint dz\frac{\hat{\sigma}(z)}{z-\omega} = 0. \tag{3.9}$$

The integral around the large semi circle is also zero, leaving

$$\int_{-\infty}^{\omega-\epsilon} dz\frac{\hat{\sigma}(z)}{z-\omega} + \int_{\omega+\epsilon}^{\infty} dz\frac{\hat{\sigma}(z)}{z-\omega} + \int_{\pi}^{0} d(\omega+\epsilon e^{i\phi})\frac{\hat{\sigma}(\omega+\epsilon e^{i\phi})}{\epsilon e^{i\phi}} = 0 \tag{3.10}$$

The first two integrals give the principle value of the integral for $\epsilon \to 0$,

$$\mathcal{P}\int_{-\infty}^{\infty} d\omega' \frac{\hat{\sigma}(\omega')}{\omega' - \omega} - \pi i \hat{\sigma}(\omega') = 0, \tag{3.11}$$

from which the Kramers-Kronig relations follow:

$$\sigma_1(\omega) = \frac{1}{\pi}\mathcal{P}\int_{-\infty}^{\infty} \frac{\sigma_2(\omega')}{\omega' - \omega} d\omega' \tag{3.12}$$

and

$$\sigma_2(\omega) = -\frac{1}{\pi}\mathcal{P}\int_{-\infty}^{\infty} \frac{\sigma_1(\omega')}{\omega' - \omega} d\omega'. \tag{3.13}$$

Using $Im(M(\tau)) = 0$ gives the relation $\hat{\sigma}(-\omega) = \hat{\sigma}^*(\omega)$, which implies that $\sigma_1(-\omega) = \sigma_1(\omega)$ and $\sigma_2(-\omega) = -\sigma_2(\omega)$. The relations can then be rewritten so that

$$\sigma_1(\omega) = \frac{2}{\pi}\mathcal{P}\int_{0}^{\infty} \frac{\omega'\sigma_2(\omega')}{\omega'^2 - \omega^2} d\omega' \tag{3.14}$$

and

$$\sigma_2(\omega) = -\frac{2\omega}{\pi}\mathcal{P}\int_{0}^{\infty} \frac{\sigma_1(\omega')}{\omega'^2 - \omega^2} d\omega'. \tag{3.15}$$

These relations between the real and imaginary parts of the optical conductivity follow from the general relations between the real and imaginary part of the causal response functions and are known as the Kramers-Kronig (KK) relations. [8]

The KK relations can be used to analyze data in reflectance experiments. The reflectivity $R(\omega)$ is related to the complex reflectivity $\hat{r}^*(\omega)$ by

$$R(\omega) = \hat{r}(\omega)\hat{r}^*(\omega). \tag{3.16}$$

The index of refraction, n, and the extinction coefficient, k, are related to the complex reflectivity by

$$\hat{r}(\omega) = \frac{(n-1+ik)}{n+1+ik}. \tag{3.17}$$

The complex reflectivity amplitude, $\rho(\omega)$ can be written as

$$\hat{r}(\omega) = \rho(\omega)e^{i\theta(\omega)}, \tag{3.18}$$

where $\theta(\omega)$ is the phase. Then reflectivity can be written as

$$R(\omega) = \rho^2(\omega). \tag{3.19}$$

The amplitude $\rho(\omega)$ is the measured intensity from the experiment. Taking the logarithm of $r(\omega)$

$$lnr(\omega) = ln\rho(\omega) + i\theta(\omega) \tag{3.20}$$

The phase may now be determined using the same arguments as for the KK relations

$$\theta(\omega) = -\frac{2\omega}{\pi}\mathcal{P}\int_0^\infty \frac{ln\rho(\omega')}{\omega'^2-\omega^2}d\omega'. \tag{3.21}$$

The absorption can then be determined from the measured reflectance. [9] The optical constants n and k can be obtained using Equation 3.17. From the values of n and k the real and imaginary parts dielectric function can then be calculated.

$$\epsilon_1 = n^2 - k^2 \tag{3.22}$$

and

$$\epsilon_2 = 2nk. \tag{3.23}$$

The real and imaginary parts of the optical conductivity can then be obtained from the dielectric function and are given by

$$\sigma_1(\omega) = \frac{\omega\epsilon_2}{4\pi} \tag{3.24}$$

and

$$\sigma_2(\omega) = \frac{\omega}{4\pi}(\epsilon_1 - 1). \tag{3.25}$$

3.2 High Tc Cuprates

The reflectance can be measured along the a-b plane or the c-axis to obtain the optical conductivity. If charge carriers begin to conduct along the c-axis after the bulk superconducting transition then a drude peak should be visible in the c-axis conductivity. C. Homes has measured the optical properties of $La_{1.875}Ba_{0.125}CuO_4$ along the a-b plane above the bulk superconducting transition temperature. [7]

Reflectivity measurements of $La_{1.875}Ba_{0.125}CuO_4$ along the a-b plane taken from the literature are presented in Figure 3.3. The reflectance shows metallic behavior. Low frequency reflectance increases with decreasing temperature and at higher frequency a plasma edge occurs with a minimum at about 8000cm^{-1}. In the range of 200-2000cm^{-1} the reflectivity decreases with decreasing temperature below 60K. This corresponds to the transition into the charge stripe state and the suppresion of reflectivity in this range is caused by this charge ordering. [7]

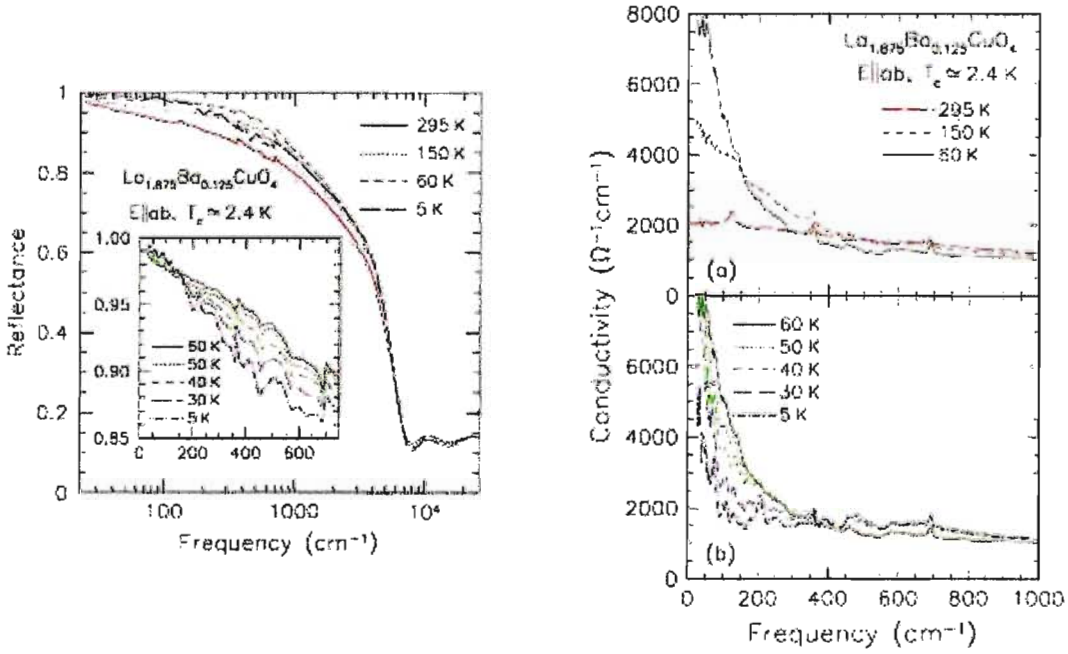

Figure 3.3: The reflectance measured over a wide frequency range from 290-5K in the a-b plane and the resulting conductivity. [7]

The optical conductivity calculated from the reflectance displays a sharp Drude peak as temperature is lowered from 295 to 60K. There is an accompanying increase in spectral weight at low frequency which is proportional to the area under the conductivity curve. This is consistent with results for $La_{2-x}Sr_xCuO_4$ [10]. Below 60K the drude peak begins to narrow and the spectral weight below 300cm^{-1} decreases.

This loss of spectral weight is redistributed to higher frequencies and is fully recovered around 2000cm^{-1}. The loss of spectral weight below 300cm^{-1} is a result of a decreasing carrier density caused by the charge stripe ordered state. This is responsible for a suppressed superconducting transition temperature of 2.4K in the $x = 0.125$ case. [7]

The reflectance of $La_{2-x}Ba_xCuO_4$ for $x = 0.125$ has been measured from 25-600cm^{-1} in the normal state along the c-axis by C. Homes and is presented in Figure 3.4.

The reflectance measured along the c-axis shows two strong absorption features which are phonons at around 600cm^{-1} and 470cm^{-1}. There are 3 small phonon features that appear as temperature decreases at 300cm^{-1}, 350cm^{-1} and 375cm^{-1}. All of these phonons increase in strength as temperature decreases. Below 200cm^{-1} the reflectance drops steadily from near unity to about 50%. In the superconducting state it is expected that a plasma edge should be apparent as a slight decrease in the reflectance followed by a sharp increase to a reflectance near 100%.

The c-axis infrared reflectivity of $La_{2-x}Sr_xCuO_4$ from 25-350 cm^{-1} is shown in Figure 3.5. The reflectivity appears almost identical to $La_{2-x}Ba_xCuO_4$ but the plasma edge is found to onset below Tc at a frequency of about 25 cm^{-1} for $x = 0.13$.

The goal of this thesis was to search for the plasma edge in the superconducting state of $La_{1.875}Ba_{0.125}CuO_4$ along the c-axis to complete analysis of the conductivity via the Kramers-Kronig relations. The far infrared region below 50cm^{-1} will be probed for the plasma edge. Several factors such as the low intensity of light sources below 100cm^{-1} make Fourier transform infrared(FTIR) spectroscopy difficult in this range. This experiment should yield valuable information on the low frequency limits of FTIR spectroscopy.

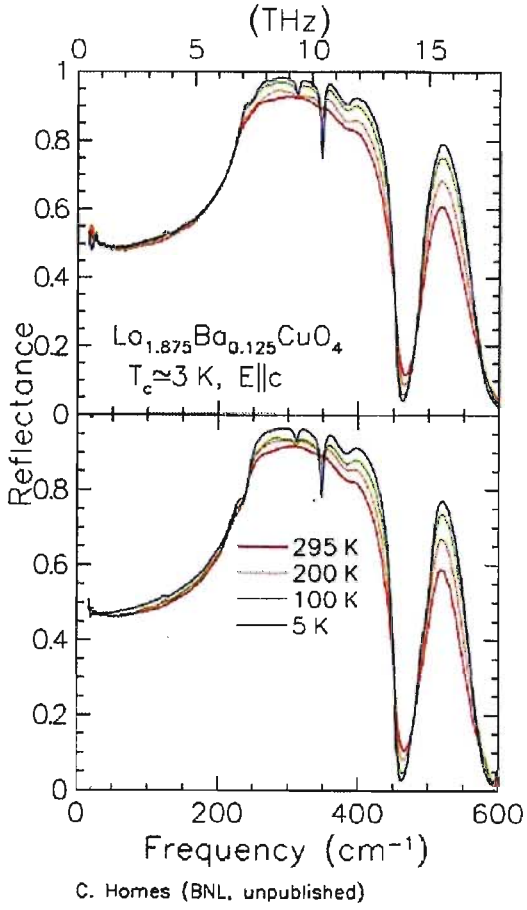

Figure 3.4: The c-axis reflectance of $La_{1.875}Ba_{0.125}CuO_4$ as measured by C. Homes at Brookhaven National Labs. The upper panel is the reflectance of a single crystal of $La_{1.875}Ba_{0.125}CuO_4$ and the lower panel is the same crystal which will be used in the experiments carried out for this thesis.

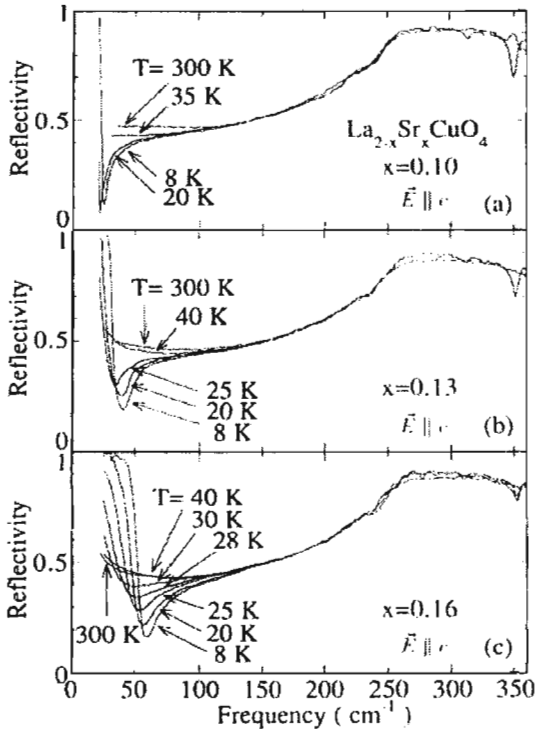

Figure 3.5: The c-axis reflectivity of $La_{2-x}Sr_xCuO_4$ for various temperatures and concentrations. (a) x=0.10 (Tc=27K) (b) x=0.13 (Tc=32K) and (c) x=0.16 (Tc=34K) [11]

Chapter 4

Experimental Method

4.1 Low Energy Spectroscopy

In the course of this thesis work, several factors such as light sources, spectrometers and filtering combinations were investigated to maximize the intensity of light measured by a detector at low frequencies. This is needed in order to have the best chance of detecting the plasma edge in $La_{1.875}Ba_{0.125}CuO_4$ which, if it exists, is believed to occur well below $50cm^{-1}$. A He^3 cryostat coupled with a Martin-Puplett spectrometer is maximized to reach the lowest frequencies possible. A Bruker rapid scan spectrometer has recently been modified to be coupled with the He^3 cryostat. Measurements taken with both systems will be reported in order to compare and optimize the low frequency reflectance measurements. That is, this project will give a comparative look at the two low frequency spectrometers with the goal of optimizing filtering and saving time in the detection of low energy features such as the plasma edge.

The optical properties of the sample at temperatures as low as 0.5K are probed using a He^3 cryostat. The cryostat creates a temperature gradient using layers of liquid nitrogen and liquid helium to isolate a detector and a sample stage which houses our sample and a reference mirror.

To probe the optical properties the cryostat is connected to either a Bruker IFS 66v/S spectrometer which employs a rapid scan technique or to a Sciencetech Martin-

Puplett polarizing spectrometer which uses a step and integrate method.

4.2 Spectrometer

Experimental measurements of the reflectance of a sample are used to determine the optical constants. Light is directed to the surface of the material at a near normal angle of incidence and then reflected to a detector. A monochromatic light source will only measure the reflectivity of one frequency. By using Fourier Transform Infra-Red (FTIR) spectroscopy the reflectance can be measured for an entire range of frequencies.

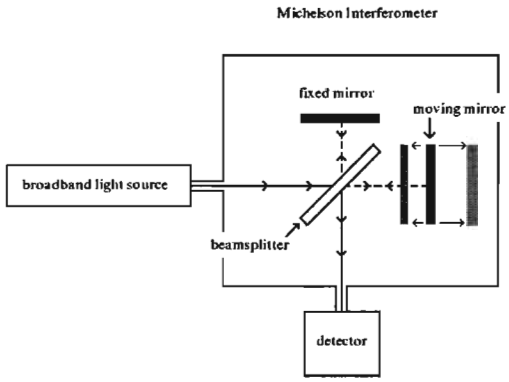

Figure 4.1: A Michelson Interferometer.

The Michelson Interferometer as seen in Figure 4.1 uses a broadband light source to measure reflectance. A broadband of infrared light is sent through a beamsplitter which sends half of the light to a fixed mirror and the other half of the light to a movable mirror. The light then reflects back to the beamsplitter and recombines on the other side. This light will be directed towards a detector. The measured light intensity from the detector will depend upon the difference in the length of travel for the two mirrors known as the optical path difference or optical retardation δ. An

interferogram, which is a measure of the intensity as a function of the path difference $I(\delta)$ is collected by the detector. By using a Fourier Transform, the interferogram and the measured optical path difference can be turned into a power spectrum, which is a measure of the intensity of the reflected light as a function of frequency.

$$I(\nu) = \int_{-\infty}^{\infty} I(\delta) cos(2\pi\nu\delta) d\delta \tag{4.1}$$

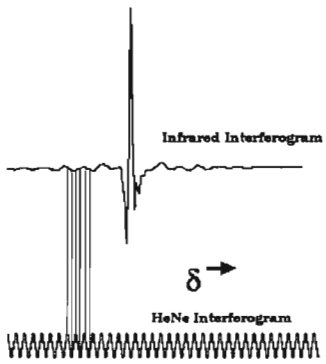

Figure 4.2: Interferogram showing the intensity vs optical path difference. The lower trace shows the interferogram generated by the laser and how the laser interferogram is used to generate the digitization points. (Figure taken from Bruker manual) [12])

4.2.1 Bruker Spectrometer

Optical measurements were taken with a Bruker IFS 66v/S spectrometer. The Bruker uses a rapid scan Michelson interferometer and a broadband light source (either a Globar^{TM} or a mercury arc lamp) to measure reflectance. The optical path difference is varied in a rapid scan spectrometer by moving one mirror at a constant velocity. When the mirrors are at the same relative position there will be a large peak in the

interferogram, as all wavelengths of light will constructively interfere. As the mirrors move further from the central peak different wavelengths will interfere constructively while others will interfere destructively. This will often produce successively smaller peaks as δ moves further from the zero path difference. The path difference is measured accurately with a helium-neon (HeNe) laser that is sent through the same beamsplitter and into a different detector. This detector will measure the intensity of interference fringes produced by the laser beam, which in turn will yield the path difference. Figure 4.2 illustrates how the laser fringes are used to measure the optical path difference of the interferogram.

4.2.2 Martin-Puplett Polarizing Spectrometer

In addition to the Bruker spectrometer, optical measurements were carried out with a Sciencetech Martin Puplett polarizing interferometer. The Martin-Puplett has a mercury arc lamp as the light source and uses a step scan method to obtain the interferogram. The moving mirror "steps" in known increments from a calibrated zero path. Light is polarized on a 45^o angle before it hits a polarizing beamsplitter. The polarizing beamsplitter then splits the light, transmitting light that is polarized perpendicular to the grid and reflecting light that is polarized parallel. The light then reflects from a ceiling mirror, which changes the polarization of light. Upon returning to the beamsplitter the reflected light will be transmitted, the transmitted light will be reflected, and the recombined beam will have components from both polarizations. Wire grid polarizers boast that the transmission of the beamsplitter is almost unity [13], but the Mylar® grid used in the Martin Puplett spectrometer reduces the intensity of the final beam slightly. A polarizing chopper modulates the signal at a controlled output frequency. The modulated signal is measured by a lock-in amplifier.

4.3 Source

The major limitation encountered in far infrared spectroscopy is the light source itself. A silicon carbide or "Globar^{TM}" source provides good data from 100cm^{-1} to 400cm^{-1}. A mercury arc lamp provides more intensity for frequencies of light below 100cm^{-1}. While approaching millimeter wavelengths the intensity of light falls off drastically with decreasing frequency. The spectral energy density of light from a blackbody at 1400K, approximately the temperature reached by the arc inside the mercury lamp, at 10cm^{-1} is known to be about 100 times weaker than at 100cm^{-1} and about 5800 times weaker than at 1000cm^{-1}. [14]

4.4 Filtering

The filtering which is chosen for an optical system will affect the intensity and frequency range of the power spectra obtained. Several different combinations of filters were tested for the far infrared range. A combination of glass and black polyethylene was found to maximize the power spectra for 6-40cm^{-1}.

The thickness of the glass is the main factor which affects the power spectra. Thicker glass cuts off the higher frequencies of light but also reduces the transmission. It is necessary to choose a thickness that will optimize the detectors response to the low frequency light. Black polyethylene does not significantly affect the spectra, but without a layer of black poly, the detector will warm above its operating temperature and it will not be possible to collect a spectrum. A filter which is composed of black polyethylene on crystaline quartz can be combined with the glass filter. Black poly can also be 'melted' onto a glass filter. It was found that the crystaline quartz did not significantly affect the intensity of the spectra.

The choice of whether to use black poly on quartz or on glass directly is made

based on other experimental details. For the thickest glass filter tested the black poly was melted directly on to the filter. The bolometer filter stage was too small to incorporate the additional quartz filter in the experimental setup. The regular glass filter was tested with both black poly melted directly to the filter and with a clean glass filter combined with a layer of black poly on crystalline quartz. It was much easier to use a layer of black poly on crystalline quartz in combination with a clean glass filter than to melt poly directly on glass. The poly does not bond easily or very well to the glass surface. For measurements with glass that is thin enough to allow an additional filter to be placed in front of the detector, it is convenient to use the additional filter made of black poly on crystalline quartz as opposed to bonding the black poly to the glass surface directly.

4.5 Detectors

Liquid Helium cooled bolometers are used to detect the infrared radiation at the lowest frequency range. Johnson noise is the limiting factor of these detectors [14]. The voltage of Johnson noise is given by

$$V_n = \sqrt{4k_b \Delta\nu RT}, \tag{4.2}$$

where k_b is the Boltzmann constant, $\Delta\nu$ is the bandwidth of the detector, R is the resistance of the bolometer and T is the operating temperature. A He^4 detector operates at about 4K and will have a low cutoff of about $20cm^{-1}$. A He^3 cooled detector will operate at 0.4K and with bandwidth restriction can reach frequencies as low as $1cm^{-1}$. [7]

4.6 Data Collection

Once a temperature of 0.4K or 4K is reached inside the cryostat, the corresponding bolometer will become operational. The far infrared light will enter the cryostat and the sample chamber, where it will reflect from either a sample or a fixed reference mirror into the bolometer chamber. Light may be filtered or polarized before it enters the bolometer chamber.

The bolometer works by measuring changes in resistance due to changes in temperature upon absorption of the far infrared light reflected from the sample or reference mirror. The bolometer response is a measure of the intensity of light versus the optical path difference. The spectrometer measures the change in path difference over time. A computer program makes use of a Fourier transform to create a graph of intensity vs frequency, known as the power spectrum, from the interferogram which represents intensity as a function of path difference. The power spectrum is a measurement of light intensity as a function of frequency of the light reflected from the sample or reference mirror. Distortions resulting from the geometry, temperature drift or optical windows are present in the measurement of a power spectrum. The intensity of the power spectrum changes with frequency as the light from the source is also frequency dependent.

Several power spectra were measured to determine the optimum experimental setup for acquiring the lowest frequency data with the highest intensity. Several different spectrometer and filtering combinations were used and are presented in Chapter 5.

Once a power spectrum is collected it needs to be normalized using a reference. For every spectrum that is collected from the sample, a spectrum is also collected from a reference mirror. This mirror is used to account for changes in the response

of the detector due to temperature drift. Once the sample has been measured, the cryostat is warmed up and a thin film of gold is evaporated onto the sample. The experiment is performed once again. The evaporation of gold is used to cancel out the influence of the geometry of the sample and the filtering. The absolute reflectance, R, is given by

$$R = \frac{sample}{reference} \times \frac{reference}{goldcoatedsample \times R(gold)}, \tag{4.3}$$

where R(gold) is often taken to be unity at low frequencies. The gold coated sample is used to eliminate features in the reflectance caused by geometry while the reference mirror eliminates changes in reflectance due to temperature drift and light intensity from the source. This provides a measure of absolute reflectance as a function of frequency for the sample.

4.7 Cryostat

A cryostat is used to house the sample and the bolometer. Cryogens, liquid helium and liquid nitrogen, combined with a vacuum layer create a temperature gradient. The vacuum layer isolates the cryogens and the sample and bolometer cold plates from the outside environment (Temperature 292K).

The cryostat is evacuated using a Varian vacuum pump. A small vacuum of 10^{-3} torr is first achieved with a roughing pump. A turbo pump on the Varian vacuum system is then switched on and a pressure of approximately 10^{-5} torr is reached. This has isolated the system and it can now be cooled.

The green valves on the He^3 gas storage tanks are opened to allow the He^3 to flow into the system (see Figure 4.3). The refrigerator and pump switches, which are metal contacts connecting to the He^4 cold plate, should be closed so that the sample

stage, bolometer stage, and both of the charcoal pumps are cooled. Liquid nitrogen (LN_2) is transferred into both the nitrogen and helium vessels. The system is now at 77K. The helium vessel is then emptied of the liquid nitrogen by applying pressure from gaseous nitrogen. The helium compartment which is now filled with nitrogen gas is flushed out with helium gas. This is done to avoid having nitrogen sublimate into a solid. Liquid helium can now be transferred into the cryostat. The system will now be around a temperature of 4K and the He^3 will be absorbed onto the charcoal in the pumps.

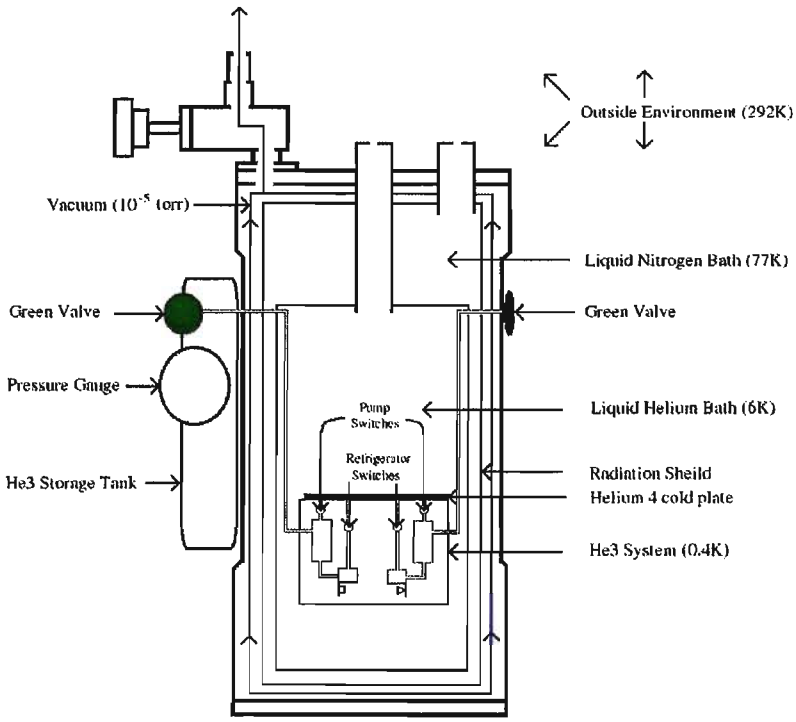

Figure 4.3: The temperature gradient inside the cryostat is created by cryogen and vacuum layers.

4.7.1 Pumping on the He^4 Bath

After allowing suitable time for the system to stabilize at 4.2K the temperature can be decreased further. The sample stage and bolometer pump switches should be opened so that the He^3 adsorbed onto the charcoal pumps can be driven off and condensed on the sample and bolometer refrigerators. This process is described in detail in section 4.7.2. Lowering the pressure by pumping on the He^4 bath with a Trivac pump will decrease the vapour pressure above the helium and therefore decrease the temperature as shown by the ideal gas law in equation 4.4. At 2.17K liquid helium passes its lambda point and becomes a superfluid.

$$PV = nRT \tag{4.4}$$

4.7.2 He^3 System

The cryostat houses a closed gas flow system which reuses He^3 in every experiment in order to reach temperatures as low as 0.4K. Two identical systems control the temperature of the bolometer and the sample stage for the 4K - 0.4K temperature range. The process is best illustrated in three stages.

Stage 1 - The charcoal pump and cold plate are connected to the helium bath and are at a temperature of 4.2K. Opening the green valves on the He^3 storage tanks will cause the gas to condense on the cold, adsorbant charcoal inside the pump, as shown in Figure 4.4

Stage 2 - The green valves are closed trapping the He^3 inside the system. The Trivac pump is turned on to pump on the He^4 bath. The pump switch is now opened, disconnecting the charcoal pump from the liquid helium bath and a voltage of 3-4 volts is applied to the charcoal pump heater. This causes the charcoal pump to

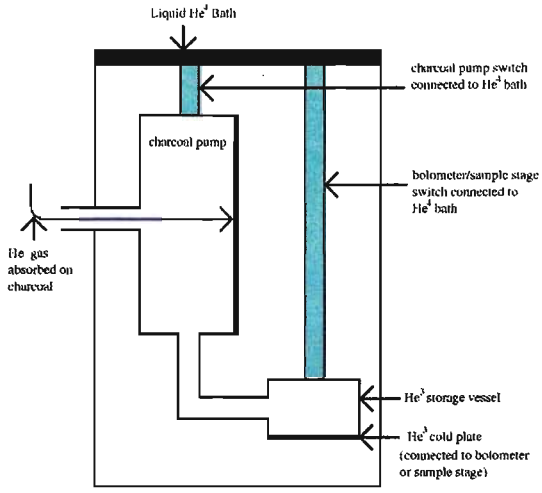

Figure 4.4: Stage 1 of the He^3 pumpdown.

slowly heat up to around 30K over the course of the pumpdown. The He^3 will now be driven off the charcoal and condense into a He^3 storage vessel where it will be at a temperature near 2K. One side of the He3 storage vessel is known as the cold plate. The sample and bolometer are mounted on these cold plates. This process is depicted in Figure 4.5

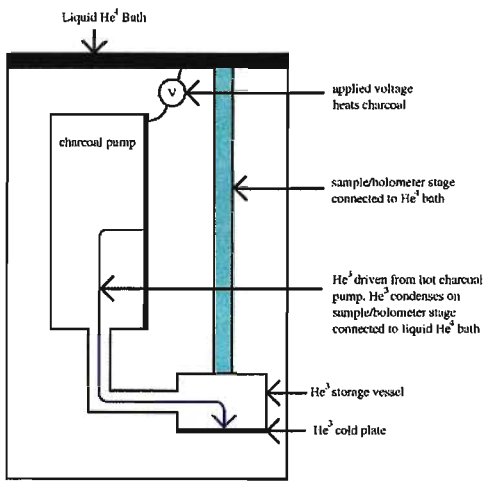

Figure 4.5: Stage 2 of the He^3 pumpdown.

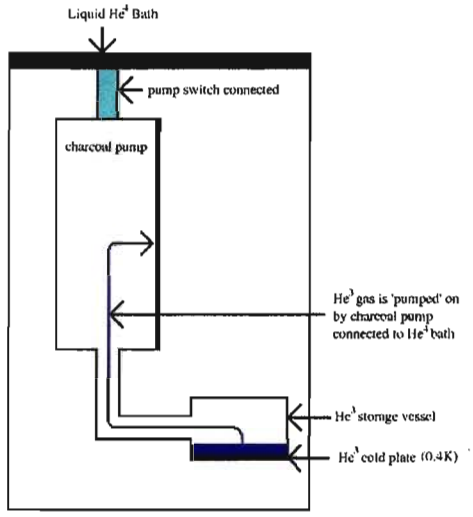

Figure 4.6: Stage 3 of the He^3 pumpdown.

Stage 3 - The power to the charcoal pump heaters is disconnected and the pumps are reconnected to the He^4 bath causing the charcoal to return to a temperature near 2K. The cold plate is then disconnected from the He^4 bath by opening the refrigerator switch. Now the He^3 gas will slowly evaporate from the condensed liquid He^3 in the chamber connected to the cold plate back onto the charcoal as shown in Figure 4.6. This "pumping" action on the liquid causes a decrease in the pressure and thus a decrease in the temperature. The liquid He^3 will now decrease in temperature to 0.4K, as will the cold plate.

4.8 Gold Evaporation

After power spectra are taken from the sample, the system must be returned to room temperature to perform an *in situ* gold evaporation. Cryo-pumping will occur which raises the vacuum inside the cryostat. The cryostat needs to be pumped on

using the Varian vacuum. A good vacuum is key to a successful gold evaporation. A tungsten filament with several small pieces of gold about 3-4mm in length and 0.25mm in diameter attached, is moved into a position which encloses the sample. A power supply is then attached to the tungsten creating a circuit. The resistance is about 1Ω. The voltage on the power supply is turned to a maximum and the current is then turned to $1A$. This will cause the gold to heat up, melt and 'bead' on the tungsten wire. The current is then increased to $2A$ causing the gold to evaporate off the tungsten wire. The pressure will increase as the gold becomes a gas. Most of the gold will condense onto the surrounding evaporator stage and the sample. The evaporator stage can then be removed and a thin layer of gold will be present on the surface of the sample.

The experiment is then repeated under the same conditions for the gold coated sample. This will provide the reference measurement and the absolute reflectance of a sample can then be calculated.

Chapter 5

Filtering

One of the goals of this thesis was to establish the best filtering to obtain measurements at the lowest frequencies and to establish a low frequency limitation to FTIR measurements in our laboratory. Several combinations of spectrometers, light sources, beamsplitters, filters and detectors were used to acquire power spectra in different spectral regions. Tables 5.1, 5.2, and 5.3 list the different conditions under which each experiment was performed. In all cases, a polarizer was present in front of the detector, polarizing light in the vertical direction, which is along the c-axis of the crystal. Figure 5.1 is a photograph of the crystal mounted to the sample stage and indicates the direction of the c-axis.

Data is collected and presented in power spectra and 100% lines. A power spectrum is a measurement of light intensity as a function of frequency of the light reflected from a sample or reference mirror. A power spectrum is a good indication of the intensity of light at the detector. The measured intensity is a voltage, but the absolute value of this voltage is dependent on several factors, such as the detector's sensitivity settings and amplifier gain. Since the measured intensity is relative to the amplification established by the experimental setup the signal to noise ratio determines the accuracy of the measured reflectance. In the power spectra presented, there are always two curves. One curve is the power spectrum of the reference mirror and one is the power spectrum of the sample. The voltage measured from the reference mirror was always higher than the voltage measured from the sample.

An easier way to illustrate the accuracy of the measured reflectance is through the use of a 100% line. This is simply a reference power spectrum that is divided by another reference power spectrum. Each 100% line in this thesis is composed of four scans, two reference measurements are divided by two other reference measurements under exactly the same experimental conditions. If the data is consistent then the result should be unity. If there is a great deviation from unity the data cannot be trusted and will not provide a reasonable measurement of the reflectivity.

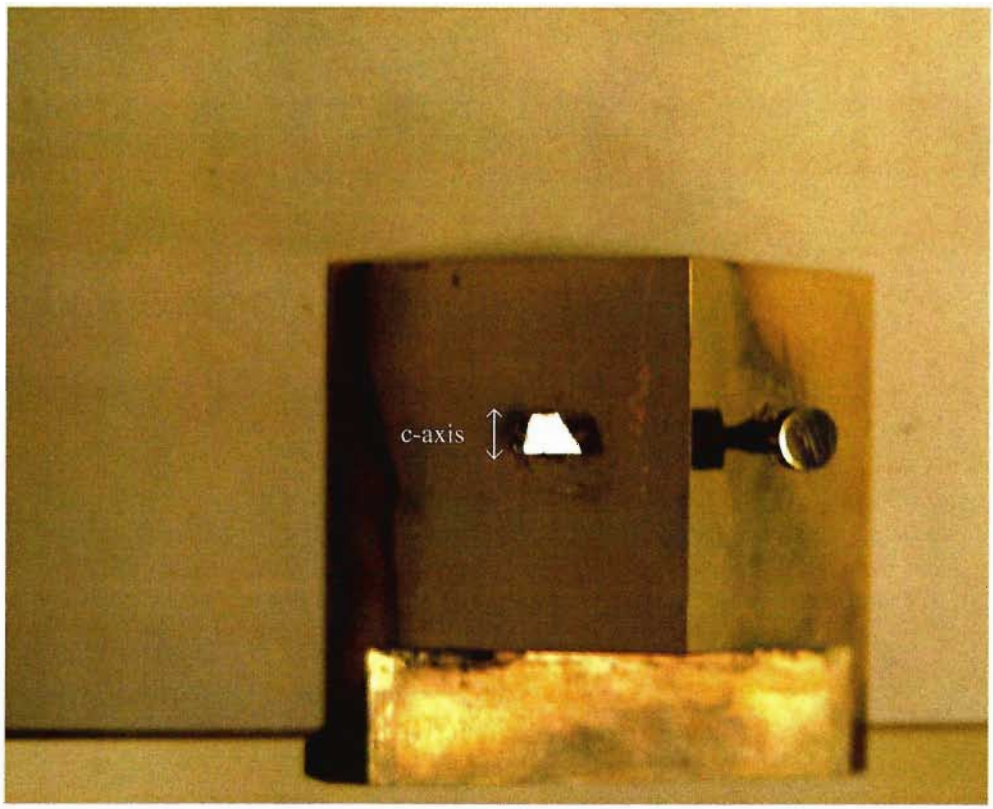

Figure 5.1: The single crystal of $La_{1.875}Ba_{0.125}CuO_4$ (on the left) with the c-axis oriented at 90° angle with respect to the polarizer. The reference mirror is shown on the right.

Experiment	1	2	3	4	5
Range	100-700cm^{-1}	100-700cm^{-1}	50-250cm^{-1}	25-125cm^{-1}	10-50cm^{-1}
Spectrometer	Bruker	M.P.	Bruker	M.P.	M.P.
Light Source	Globar	Hg arc lamp	Globar	Hg arc lamp	Hg arc lamp
Beamsplitter	6 micron	mylar polarizer	6 micron	mylar polarizer	mylar polarizer
Windows	pp. film	pp. film	quartz	quartz	quartz
Light Pipe Filtering	polyethylene plastic with b.p. on 1 side	polyethylene plastic with b.p. on 1 side	b.p. on crystal quartz	b.p. on crystal quartz	b.p. on on crystal quartz
Bolometer	4K	4K	0.4K	0.4K	0.4K
Bolometer Filtering	no filter	no filter	diamond dust and b.p. on c.q.	b.p. on c.q.	fluorogold and b.p. on c.q.

Table 5.1: Different spectrometers, beamsplitters and filter combinations used to collect data. Note b.p. = black polyethylene, c.q. = crystalline quartz, pp. = polypropylene, M.P. = Martin-Puplett

Experiment	6	7,8,9,10*	11	12	13
Range	10-50cm^{-1}	5-30cm^{-1}	5-30cm^{-1}	5-20cm^{-1}	10-20cm^{-1}
Spectrometer	Bruker	M.P.	Bruker.	M.P.	Bruker
Light Source	Hg arc lamp	Hg arc lamp	Hg arc lamp	Hg arc lamp	Hg arc lamp
Beamsplitter	50 micron	mylar polarizer	50 micron	mylar polarizer	50 micron
Windows	quartz	quartz	quartz	quartz	quartz
Light Pipe Filtering	b.p. on crystal quartz	b.p. on crystal quartz	b.p. on crystal quartz	b.p. on crystal quartz	b.p. on on crystal quartz
Bolometer	0.4K	0.4K	0.4K	0.4K	0.4K
Bolometer Filtering	fluorogold and b.p. on c.q.	2.5 mm glass slab with b.p. *(see Table 5.3)	2.5 mm glass slab and b.p. on c.q.	b.p. bonded to 5 mm glass slab	1 mm microscope slide and b.p. on c.q.

Table 5.2: Different spectrometers, beamsplitters and filter combinations used to collect data. Note b.p. = black polyethylene, c.q. = crystalline quartz pp. = polypropylene, M.P. = Martin-Puplett

Experiment	Bolometer Filtering
7	only a 2.5mm glass slab is placed in front of the detector; heating caused the bolometer to fail
8	black polyethylene is bonded to one side of the 2.5 mm glass slab; there is no crystalline quartz
9	black polyethylene is bonded to both sides of the 2.5 mm glass slab; there is no crystalline quartz
10	2.5mm glass slab and black polyethylene on crystalline quartz

Table 5.3: Experiments 6-10 are carried out with the conditions specified in Table 5.2 but with different combinations of black polyethylene.

5.1 High Frequency Measurements

In Experiment 1, high frequency measurements were made with a 4K detector and a Globar^{TM} in the Bruker spectrometer. In Experiment 2 high frequency measurements were made with a 4K detector and a mercury arc lamp in the Martin-Puplett spectrometer. Power spectra for these experiments are presented in Figure 5.2 and Figure 5.3 respectively. Figure 5.4 contains the 100% lines for the high frequency spectral ranges and also includes a low frequency measurement for comparison. The same filtering combinations were used with both spectrometers. The Bruker spectrometer produces power spectra that are more consistent and have a better signal to noise ratio in the 0-350cm^{-1} range. The light source inside the Bruker can be changed from an arc lamp to a silicon carbide, or Globar^{TM} which emits light with intensities in the mid-infra red region. The Martin Puplett is optimized for low frequency measurements and is equipped with a mercury arc lamp as the only available light source. Mercury arc lamps produce less intensity than a globar above 100-200 wavenumbers [14]. Without modification to the light source of the Martin-Puplett Spectrometer

data desired above $100cm^{-1}$ should be collected using the Bruker spectrometer.

The Globar^{TM} should give intensity for a broad range of high frequency light, but the intensity of light detected in Experiment 1 drops substantially after about $300cm^{-1}$. This is caused by either the polypropylene windows or more likely the black poly on plastic which shields the cryostat from the outside environment. A new material to shield the cryostat but to allow high frequency light is needed for reflectance measurements at higher frequencies in the He^3 cryostat. Germanium is one material that is known to transmit light of higher frequency. [14] In the future it may be useful to try using germanium windows to measure reflectance with frequencies above $300cm^{-1}$ using the Bruker spectrometer and the He^3 cryostat.

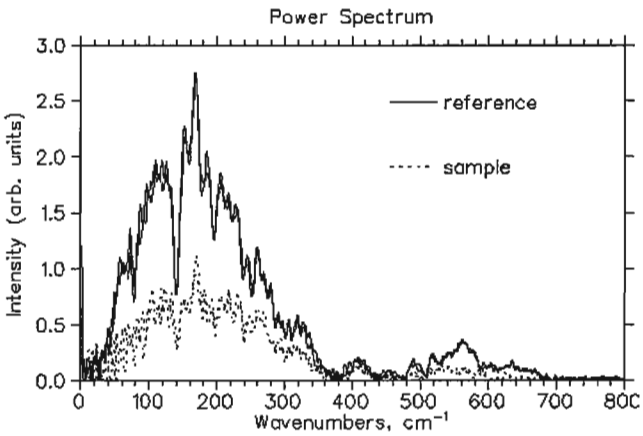

Figure 5.2: Experiment 1 - High frequency power spectrum as measured with the Bruker spectrometer.

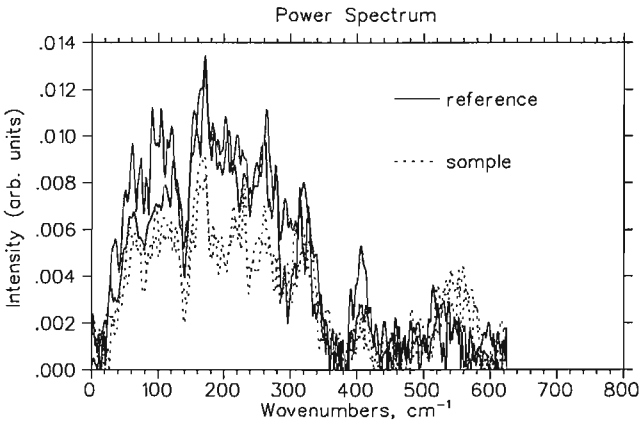

Figure 5.3: Experiment 2 - High frequency power spectrum as measured with the Martin-Puplett spectrometer.

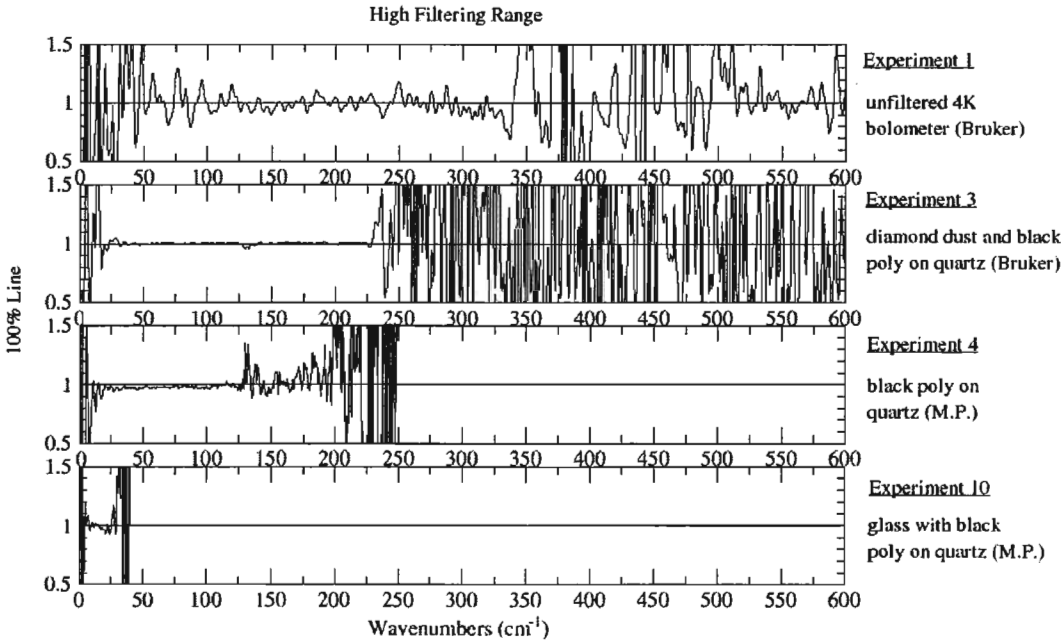

Figure 5.4: 100% lines for the high frequency spectral ranges (Experiments 1,3 and 4) and also a low frequency range (Experiment 10) for comparison.

5.2 Diamond Dust Measurements

In Experiment 3 the Bruker spectrometer is combined with the 0.4K detector, a diamond dust filter and black poly on crystal quartz to obtain data for the 50-250cm^{-1} range. The power spectra obtained in this range are presented in Figure 5.5 and show a large, consistent signal with a high signal to noise ratio. The 6 micron Mylar® beamsplitter used for this range has an absorption peak at about 130cm^{-1} which can be seen as a large decrease in the power spectra at this frequency. The 100% line for this experiment is included in the high frequency spectral range in Figure 5.4

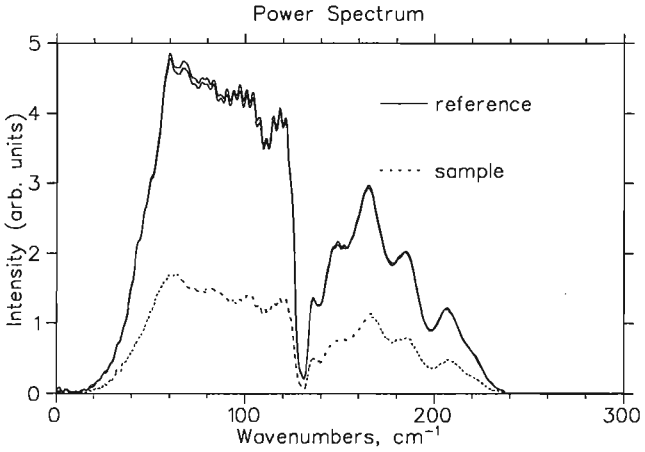

Figure 5.5: Experiment 3 - Power Spectra from the Bruker with a diamond dust filter.

5.3 Fluorogold Measurements

Fluorogold combined with black poly on quartz was used as a filter for 10-50cm^{-1} with the Martin-Puplett spectrometer in Experiment 5 and the Bruker spectrometer in Experiment 6. The power spectra are presented in Figure 5.6 and Figure 5.7 respectively. Figure 5.8 illustrates the 100% lines in and around the fluorogold range. Data for absolute reflectance was taken with the Bruker spectrometer in Experiment

6 but a problem with the sample stage caused a poor gold evaporation. The rod connecting the gold evaporator box to the control rod outside of the cryostat got stuck before the gold evaporator fully enclosed the sample. The gold evaporated over the sample and also over part of the reference mirror and as a result the reflectance could not be obtained. Thermal reflectance measurements using the Bruker are presented in the thermal reflectance section. The 100% lines for this range (see Experiments 5 and 6 in Figure 5.8) indicate that the Bruker provides a better signal to noise ratio from 30-50cm^{-1} while the Martin-Puplett is better in the 5-30cm^{-1} range. This experiment indicates that for data above 30cm^{-1} the Bruker should be the spectrometer of choice. It is also worth noting that the sample power spectrum from the Bruker is less than 50% of the reference spectrum, whereas the sample power spectrum from the Martin-Puplett is only slightly lower than the reference spectrum. This suggests that the light pipes connecting the Bruker spectrometer to the He^3 cryostat may deliver more infrared light to the reference path. It may be possible to increase the signal size from the sample by adjusting how the light from the Bruker enters the He^3 cryostat.

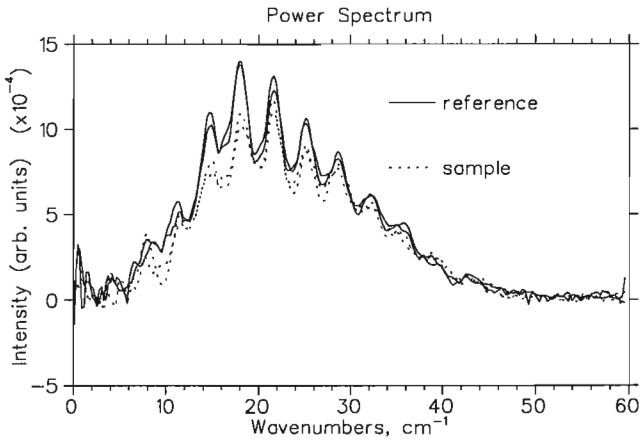

Figure 5.6: Experiment 5 - Power Spectra from the Martin-Puplett with a fluorogold filter.

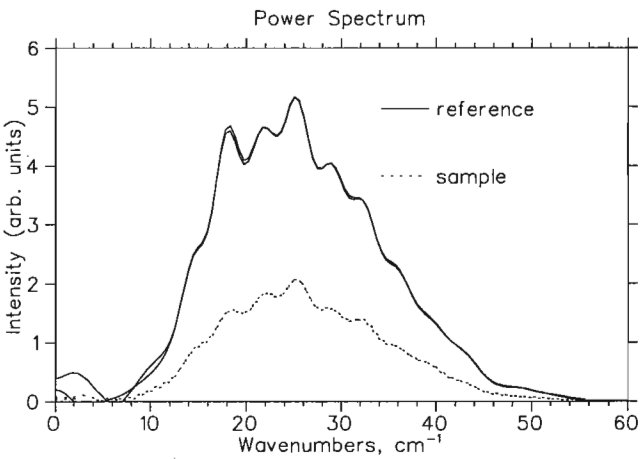

Figure 5.7: Experiment 6 - Power Spectra from the Bruker with a fluorogold filter.

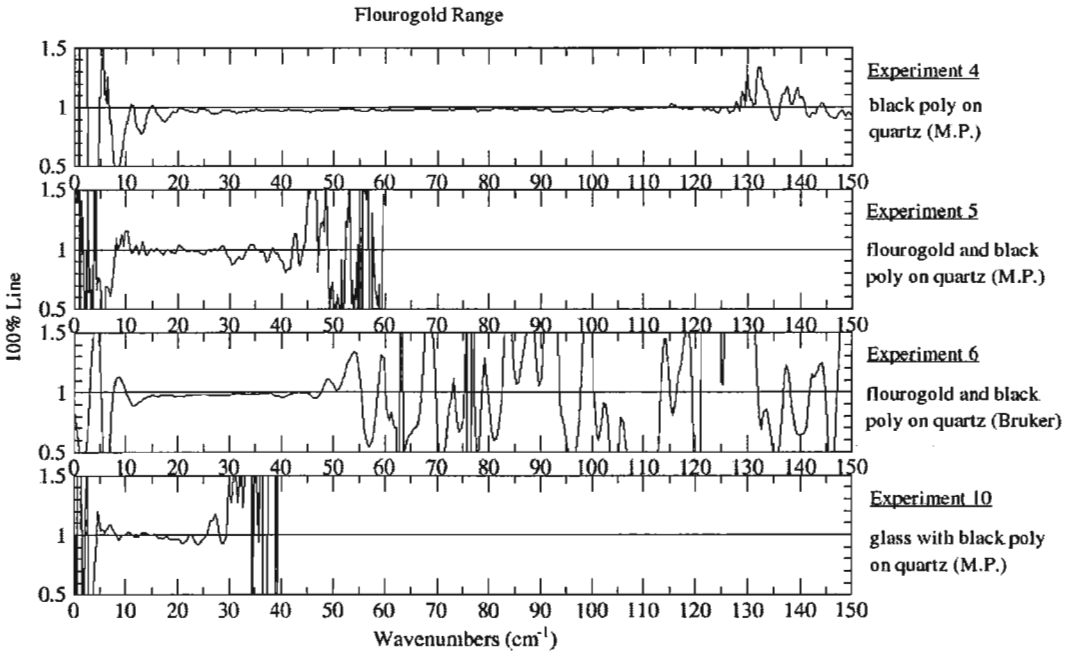

Figure 5.8: 100% lines around the fluorogold range.

5.4 Low Frequency Measurements

Glass combined with black poly is used to collect low frequency spectra. A mercury arc lamp is used as the source. The power spectra illustrating the intensity of low frequency light from the mercury arc lamp reaching the sample stage was measured in Experiment 4 and shown in Figure 5.9. The 100% line in Figure 5.8 shows that this filtering on the Martin-Puplett spectrometer provides a consistent signal for the 25-125cm^{-1} range.

The largest signal was measured in Experiment 4 with only black poly on crystalline quartz in front of the 0.4K detector. The large bandwidth reduces the sensitivity of the detector at low frequency and so to collect low frequency data a circular slab of silica borate (glass) is placed between the black poly and the detector. The

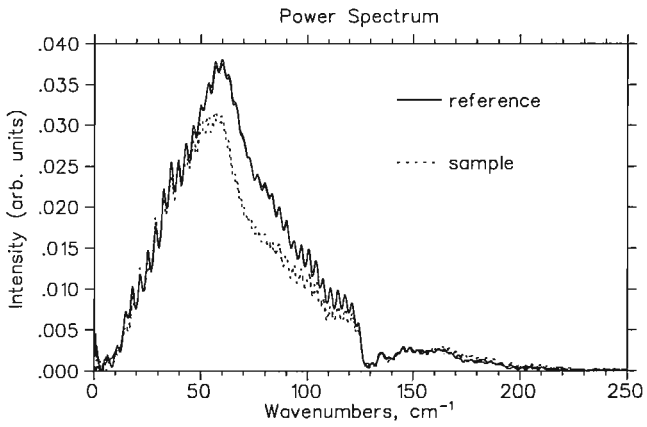

Figure 5.9: Experiment 4 - The intensity of light from the mercury lamp in the Martin Puplett Spectrometer.

thickness of glass determines the high end cutoff, with the thicker glass cutting out the higher frequencies of light. Spectra were taken with 1mm, 2.5mm, and 5mm glass slabs in order to determine the optimal thickness for low frequency measurements. The low frequency spectra are taken with the Bruker and Martin-Puplett spectrometer to confirm the conclusion made in the fluorogold range that the Martin-Puplett will preform better at low frequency. Different combinations of black poly and quartz were tested in Experiments 7-10 with the 2.5mm glass slab in order to determine the arrangement that would maximize signal intensity.

5.4.1 Black Poly and Quartz

Experiments 7-10 were carried out with the same beamsplitter, windows, light pipe filtering, bolometer, amplification settings, and with the same current applied to a mercury arc lamp. The same 2.5mm glass slab is present in front of the 0.4K bolometer in each of the experiments. The Martin-Puplett spectrometer is used in experiments 7-10. The difference between these experiments is the way that black

poly is introduced into the bolometer filtering. Figure 5.10 shows the measurements taken under the conditions specified in Experiment 7, with only a 2.5mm thick piece of glass in front of the 0.4 K detector. One power spectrum was collected before the signal died off. This illustrates that the black poly is required to prevent the heating of the 0.4K bolometer.

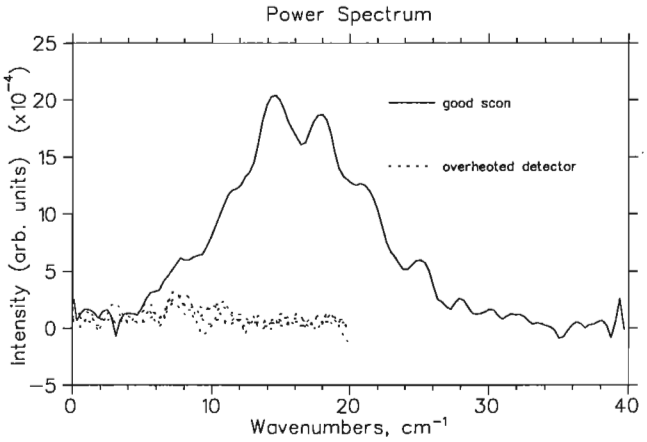

Figure 5.10: Experiment 7 - Power spectra from the Martin-Puplett with 2.5mm glass and no black poly. One scan has managed to capture a power spectrum before the bolometer dies off from heating. The other 4 scans show the detector has died off and is unable to collect any spectra. The Martin-Puplett spectrometer collects data from the failed detector below $20cm^{-1}$ but does not collect the spectrum from 20-40cm^-1 range for an unknown reason after the detector fails.

In Experiment 8 black polyethylene was melted onto one side of the same 2.5mm glass slab. Power spectra could be collected without loosing the signal due to heating and are shown in Figure 5.11. There was an increase in signal size compared to Experiment 7. It is likely that the sensitivity of the detector was affected by the lack of black poly in Experiment 7, causing the signal to be weaker.

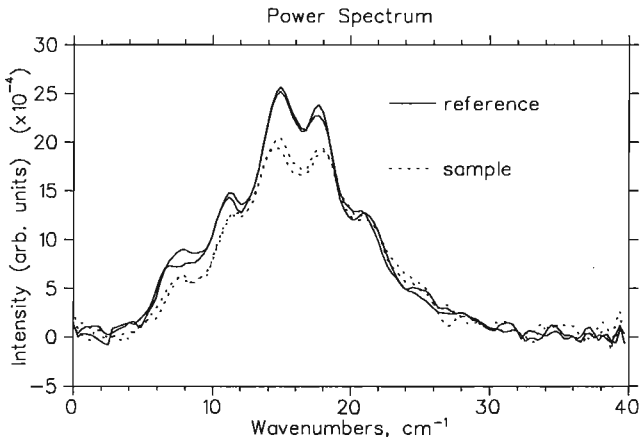

Figure 5.11: Experiment 8 - Power spectra from the Martin-Puplett with 2.5mm glass and black poly bonded to one side.

In Experiment 9 black poly is applied to both sides of the same glass disk and the power spectra can be seen in Figure 5.12. This produced similar results to Experiment 8, but there is a slight increase in intensity over the results for the black poly on one side shown in Figure 5.11. This indicates that some pin holes may be present in the black poly on the surface of glass. When black poly is only applied to one side of the glass the detector experienced some heating, decreasing the sensitivity.

In Experiment 10 data was taken with a 2.5mm thick piece of plain glass and a filter consisting of black polyethylene on crystalline quartz. Results are shown in Figure 5.13. A slight decrease in signal size is observed when compared to the glass coated with black poly on two sides. This indicates that crystal quartz has a small absorption of infrared radiation in this frequency range. The decrease in signal size is on the order of 5%.

After Experiments 7-10 it was concluded that black poly is necessary to prevent heating of the detector. Adding more layers of black poly in front of the detector does not affect the shape of the spectrum as there are already several layers of black poly

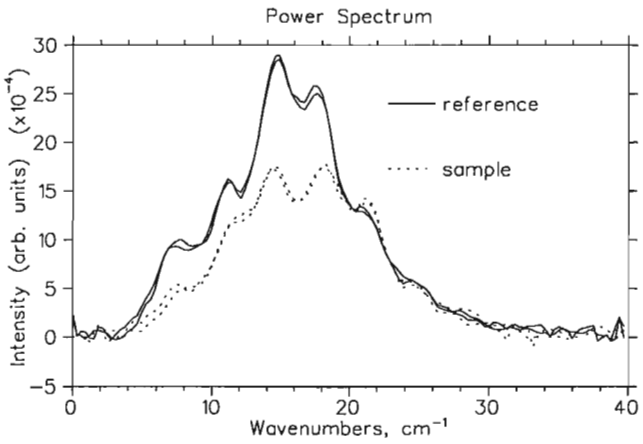

Figure 5.12: Experiment 9 - Power spectra from the Martin-Puplett with 2.5mm glass and black poly bonded to both sides.

in the lightpipes. Adding more black poly in front of the bolometer better protects the bolometer from heating and increases the measured intensity. In the future more layers of black poly could be added to determine the thickness of black poly which will maximize the sensitivity of the detector This could also provide insight into how black poly reduces signal intensity.

Adding crystal quartz has no noticeable effect on the shape of the power spectrum since there are already two such filters in the light pipes. Crystal quartz slightly decreases the intensity of the measured signal and is not necessary in front of the bolometer for collecting the lowest frequency spectra.

In Experiment 11, the same filtering is used as in Experiment 10, but the Bruker spectrometer is used to collect the data. Results for this experiment are presented in Figure 5.14. The power spectra measured with the Bruker are less consistent than the power spectra measured with the Martin-Puplett. Using the Bruker also results in a smaller frequency range than with the Martin-Puplett.

Figure 5.15 summarizes the consistency of the different arrangements of black

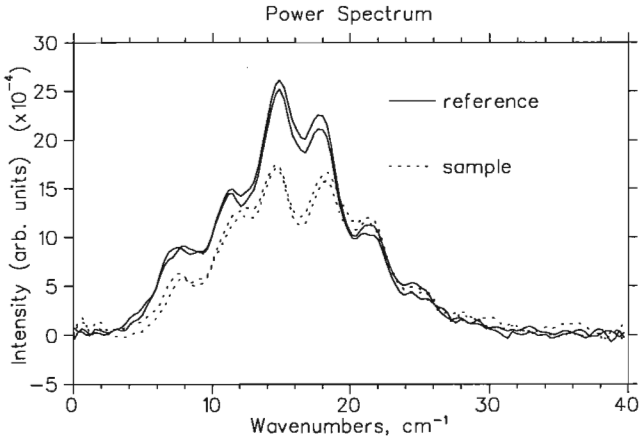

Figure 5.13: Experiment 10 - Power spectra from the Martin-Puplett with 2.5mm glass and black poly on crystal quartz.

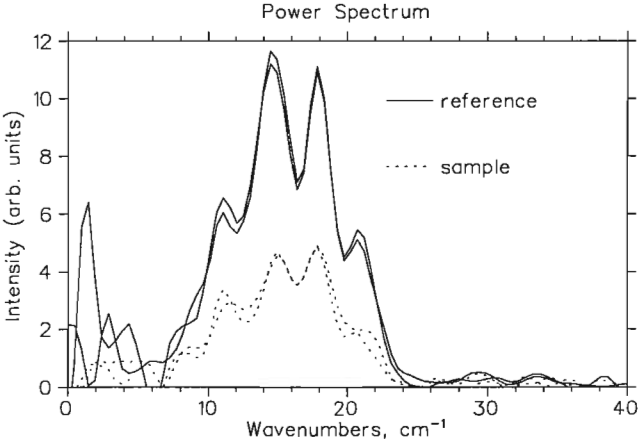

Figure 5.14: Experiment 11 - Power spectra from the Bruker with 2.5mm glass and black poly on crystal quartz.

poly and 2.5mm glass measured by the Martin-Puplett and Bruker spectrometers with 100% lines. The Martin-Puplett spectrometer measures reliable data to $6cm^{-1}$ while the Bruker only measures reliable data to $10cm^{-1}$. The Bruker also stops giving reliable data above $23cm^{-1}$ while the Martin-Puplett can provide reliable data to $30cm^{-1}$. This confirms the hypothesis that the Martin-Puplett spectrometer performs better in the lower frequency range (below about $30cm^{-1}$) while the Bruker is a better spectrometer for collecting high frequency data.

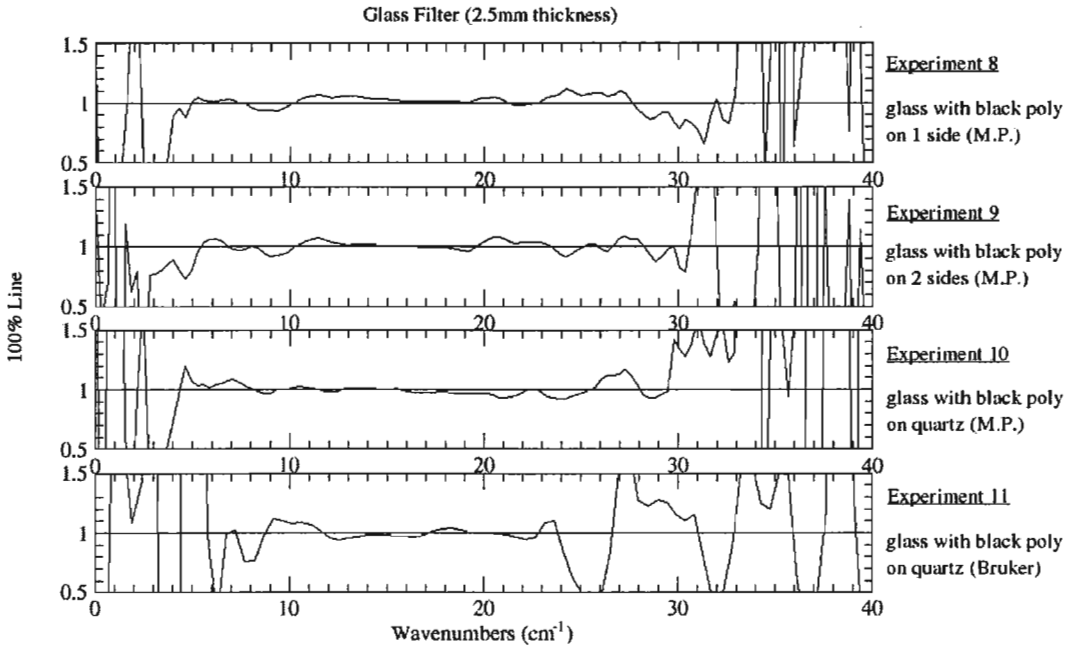

Figure 5.15: 100% lines taken with the 2.5mm glass filter(Experiments 8-11).

5.4.2 Glass Thickness

A thicker glass filter (about 5mm in thickness) was tested in Experiment 12. Higher frequencies will be cut out with the 5mm glass increasing the sensitivity of the detector but the thicker glass will decrease the signal size. The results for Experiment 12 are presented in Figure 5.16. Although the higher frequencies are cut out of the spectrum, the low frequency signal remains at a similar intensity when compared to that of the 2.5mm glass and so the 2.5 mm glass filter was used to carry out further low frequency experiments.

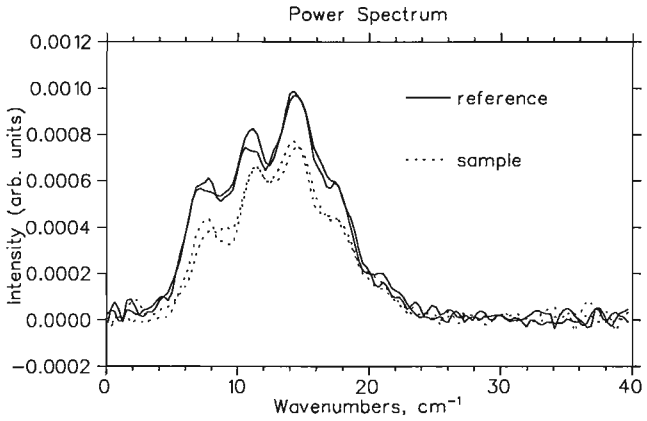

Figure 5.16: Experiment 12 - 5mm thick glass with black poly bonded to both sides.

A 1mm microscope slide was also used as a low frequency filter in Experiment 13. The power spectrum for the microscope slide is compared to the power spectrum of the 2.5mm thick glass filter in Figure 5.17. The microscope slide is likely a different type of silica borate which does not have as high a transmittance as the 2.5mm and 5mm glass.

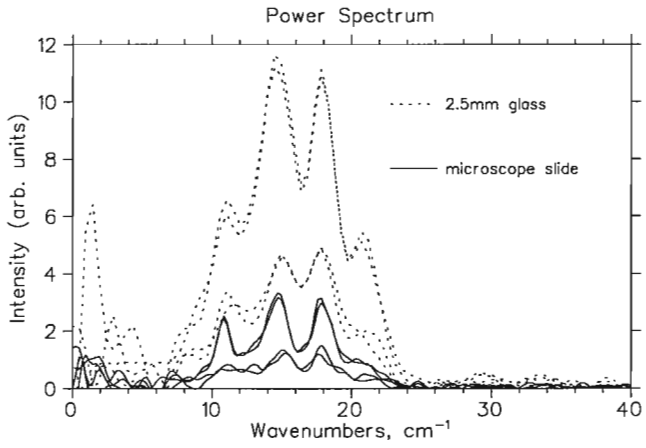

Figure 5.17: Comparison of microscope slide(Experiment 13) and 2.5mm glass(Experiment 11) as filters with the Bruker. The signal size from the microscope slide filtering is smaller for the sample and reference measurements.

A comparison between the unfiltered signal, the 2.5mm filter, the 5mm filter and the 1mm microscope slide using 100% lines is given in Figure 5.18.

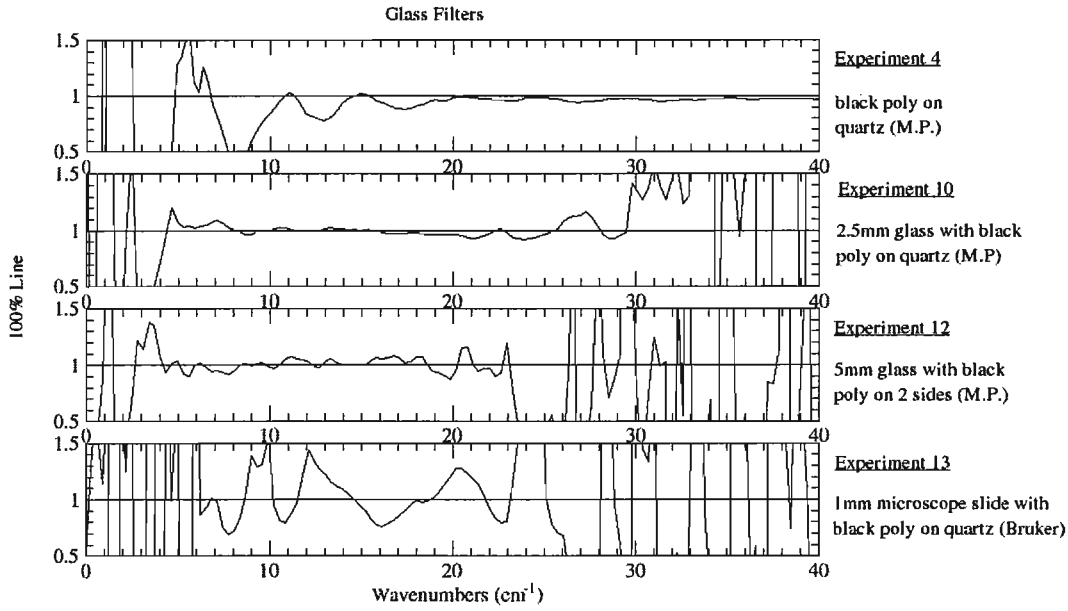

Figure 5.18: 100% lines taken with the Martin-Puplett spectrometer for glass filters of different thickness. The thin microscope slide which was only measured with the Bruker spectrometer is also shown.

5.4.3 Signal Intensity

A comparison of the power spectra from the unfiltered signal, the 2.5mm filter and the 5mm filter is presented in Figure 5.19. Figure 5.20 is a blow up of the low frequency region where the glass filters transmit light. In Figure 5.19 and Figure 5.20 the settings for sensitivity, the current applied to the arc lamp and the amplification are all the same and so this is a good illustration of how small the signal size is at low frequency. These are also good graphs for illustrating how the intensity of light from a mercury arc lamp rapidly decreases below $50cm^{-1}$. One of the biggest challenges for obtaining a good measurement of reflectance in the far infrared range is the strength of the light source.

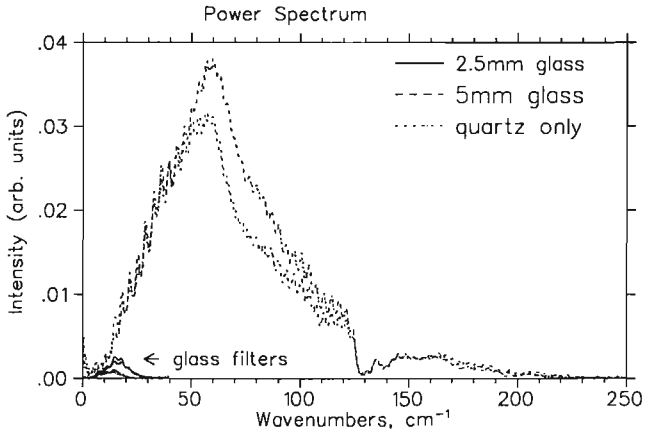

Figure 5.19: Comparison of filtering measured with the Martin-Puplett spectrometer illustrating the small signal size in the low frequency region of interest(Experiments 4,10,12). A blow up of the power spectra for the glass filters is provided in Figure 5.20

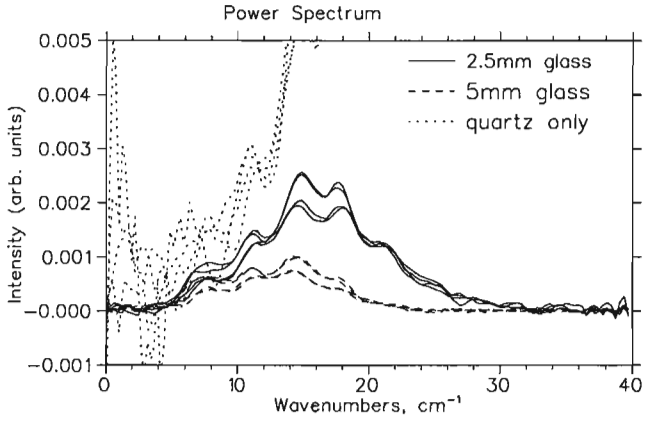

Figure 5.20: Comparison of filtering at low frequency(Experiments 4,10,12). This is a blow up of the low frequency region of Figure 5.19

Chapter 6

Optical Properties of $La_{1.875}Ba_{0.125}CuO_4$

6.1 Thermal Reflectance

The ratio of power spectra taken from the sample at 0.5K and 6K yields the thermal reflectance, R(T), given by

$$R(T) = \frac{sample0.5K}{reference0.5K} \times \frac{reference6K}{sample6K}. \tag{6.1}$$

A gold evaporation is not used to obtain the thermal reflectance since the effects due to geometry are cancelled out by dividing the two sample measurements.

Thermal reflectance measurements were obtained for $La_{1.875}Ba_{0.125}CuO_4$ from 6-230cm^{-1} and are presented in Figure 6.1. The peak in the thermal reflectance at 130cm^{-1} is caused by the absorption of the 6 micron Mylar beamsplitter and is not a real feature. At low frequency there is no evidence of a plasma edge which would be characterized by a slight drop in thermal reflection followed by a large upturn as frequency decreases. Figure 6.2 shows the thermal reflectance at low frequency measured with the Bruker and fluorogold filtering and the Martin-Puplett and glass filtering. The thermal reflectance shows no indication of a plasma edge for the range of 6 - 25 cm^{-1}(measured by the Martin-Puplett spectrometer.) Thermal reflectance

from the Bruker spectrometer and fluorogold filtering corroborates this conclusion for data in the 15-50 cm^{-1} range.

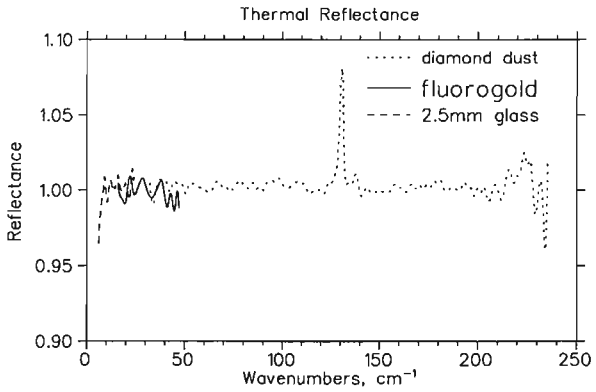

Figure 6.1: Thermal reflectance of $La_{1.875}Ba_{0.125}CuO_4$ dividing below(0.5K) by above(6K) Tc. Figure 6.2 shows a blow up of the low frequency region.

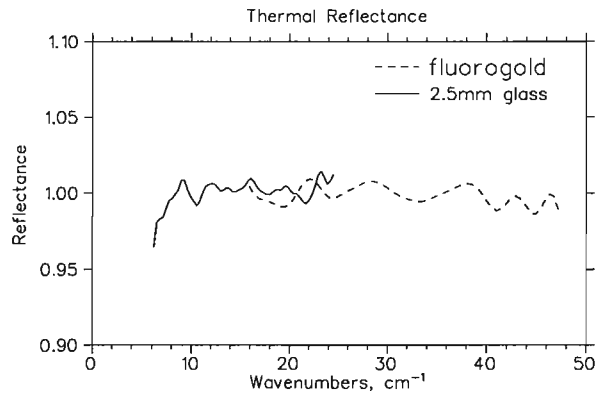

Figure 6.2: Thermal reflectance of $La_{1.875}Ba_{0.125}CuO_4$ at low frequency dividing below(0.5K) by above(6K) Tc. The drop in the thermal reflectance is likely a result of the lack of intensity from the arc lamp at the lowest frequencies.

6.2 Absolute Reflectance

Results for the absolute reflectance of $La_{1.875}Ba_{0.125}CuO_4$ were obtained and are presented in Figure 6.3. The spike in reflectance at 130cm^{-1} in the data taken at 6K is a result of the Mylar® absorption. The reflectance drops from 80% at 230cm^{-1} to a minimum of 60% at 100cm^{-1} followed by a slight rise in reflectance. This result shows an increase in the magnitude of reflectance at the minimum from the previous data obtained by C. Homes.(See Figure 3.4) In the previous data the reflectance drops to about 50%, 10% lower than in this experiment and does not begin to rise after this minimum. Initially a slight misorientation of the crystal was believed to have allowed a small contribution from the a-b plane reflectance (which is approximately 1 for this range) to increase the reflectivity. Upon re-orientation of the crystal, however, measurements in the 10-30cm^{-1} range made with the Bruker Spectrometer in Experiment 13 match the higher reflectance value.

Data was also taken for the low frequency range of 6-40cm^{-1}, however, measure-

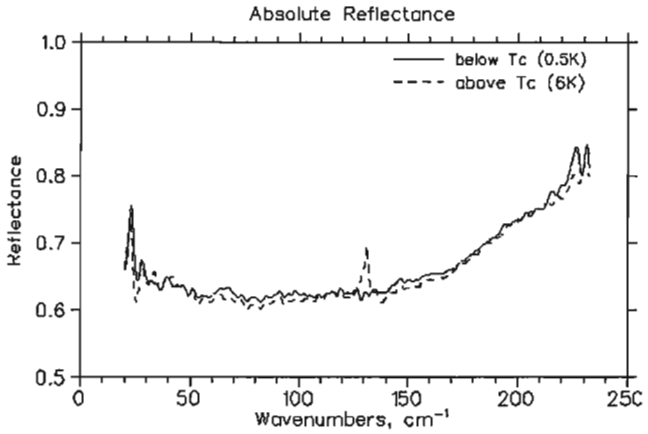

Figure 6.3: Absolute reflectance of $La_{1.875}Ba_{0.125}CuO_4$ along the c-axis. The filtering used is as described in Experiment 3.

ments of the absolute reflectance using the Martin-Puplett spectrometer were problematic as the polarizing chopper motor had to be replaced between the sample and gold coated measurements. Results for this experiment are presented in Figure 6.4 Further problems arose when the interferometer stepper motor did not respond as expected in a subsequent experiment, causing a shift in the zero path and phase. The results for absolute reflectance may thus contain errors from an inconsistent background spectrum and therefore it is possible that the contributions from geometry are not all removed. Absolute reflectance was also measured using the Bruker spectrometer in the 10-30cm^{-1} range. Data is presented in Figure 6.5 but a smaller signal to noise ratio with the Bruker spectrometer at low frequencies has resulted in reflectance measurements with greater error. Regardless of the experimental difficulties, each experiment has confirmed an increase in the magnitude of the reflectance from that measured by Homes. Each experiment also confirms that the reflectance is increasing with decreasing frequency below 50cm^{-1}.

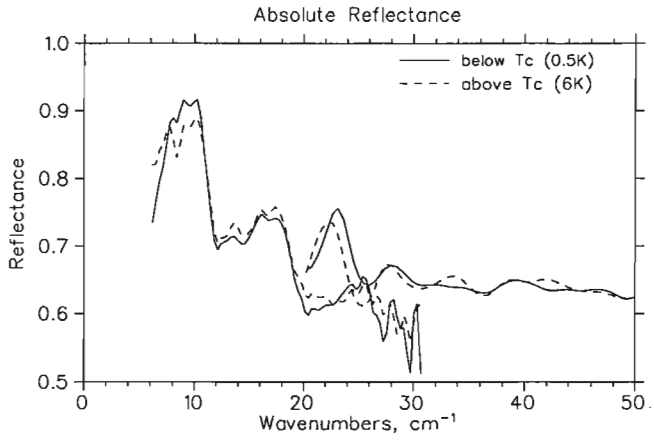

Figure 6.4: The curve on the right side of the graph is data from Figure 6.3 and is shown to roughly match the data for absolute reflectance measured with the Martin-Puplett spectrometer even though there was a chopper motor problem.

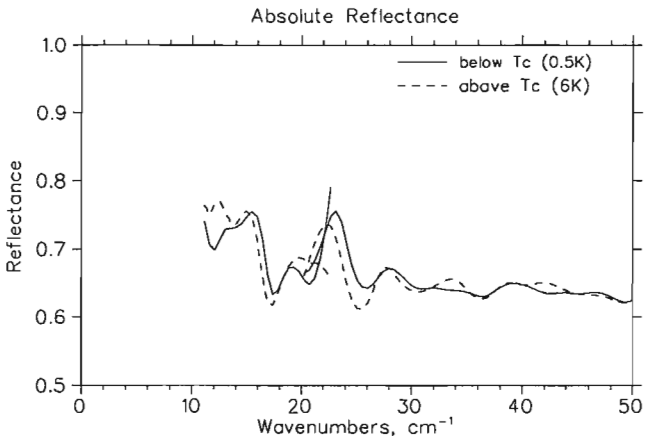

Figure 6.5: The curve on the right side of the graph is data from Figure 6.3 and is shown to match the data for absolute reflectance measured with the Bruker spectrometer

Data from Figure 6.4 was averaged and interpolated to smooth out sharp features which were believed to be artifacts of experimental difficulties. This data along with the reflectance from Figure 6.3 were used to calculate the optical conductivity via Kramers-Kronig analysis. Reflectance from C. Homes was digitized and used for the 200-600cm^{-1} range. Reflectance from La_2CuO_4 was digitized and used for the 600-26000cm^{-1} range [15]. A Hagen-Rubens approximation was used for the low frequency data and a free electron model with ω^4 was used to extrapolate data above 30000cm^{-1}. The reflectance spectrum that was used to calculate the conductivity is presented as a function of frequency on a logarithmic scale in Figure 6.6. Figure 6.7 is the reflectance used to calculate the conductivity in the 0-550cm^{-1} region.

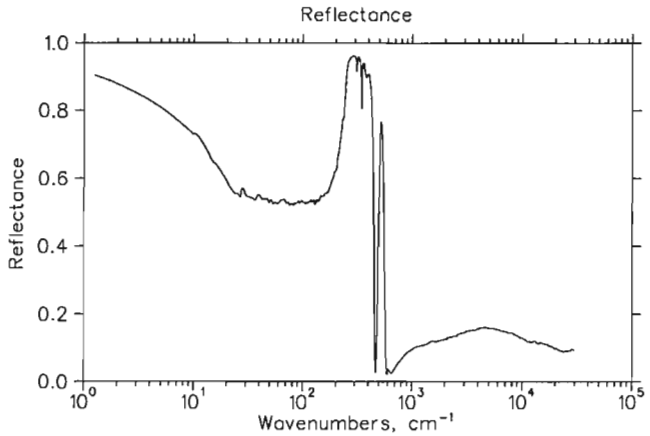

Figure 6.6: Reflectance of $La_{1.875}Ba_{0.125}CuO_4$ at 6K on a logarithmic scale showing the digitized data up to 30000cm^{-1}

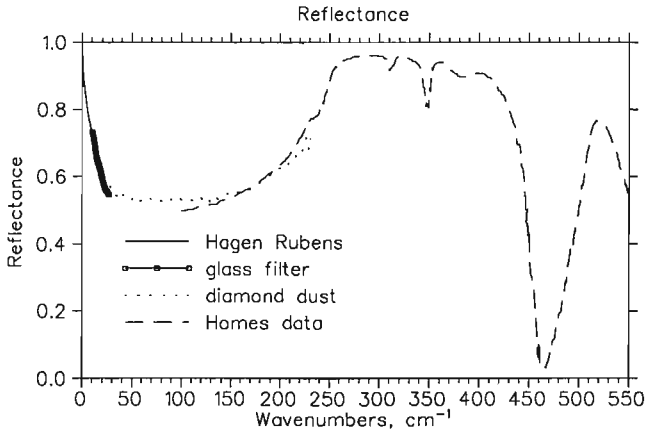

Figure 6.7: Reflectance of $La_{1.875}Ba_{0.125}CuO_4$ at 6K. In regions of overlap an averaging routine was used before Kramers-Kronig analysis.

6.3 Conductivity

Kramers-Kronig analysis was performed with data that was both above(6K) and below(0.5K) the bulk superconducting transition for the 6-250cm^{-1} range. The digitized data in the 250-26000cm^{-1} range was taken above the bulk superconducting transition. The resulting conductivity is presented in Figure 6.8. No significant changes were observed above and below Tc in the conductivity curve. Since there are several phonons present in the 250-600cm^{-1} range it is possible that the superconducting transition could affect the behaviour of these phonons and hence the true conductivity curve may differ from what is shown above 250cm^{-}1.

There are several sharp features that appear in the conductivity curve. A small peak appears at 315cm^{-1} and another which is attributed to a phonon at 350cm^{-1}. Two larger peaks appear at 500cm^{-1} and 220cm^{-1} and can also be attributed to phonons. Since extrapolations were used for data below 6cm^{-1} any potential phonons or features in this range would not be present in the data. Below 220cm^{-1} the conductivity decreases with decreasing frequency. The region contains no features to sug-

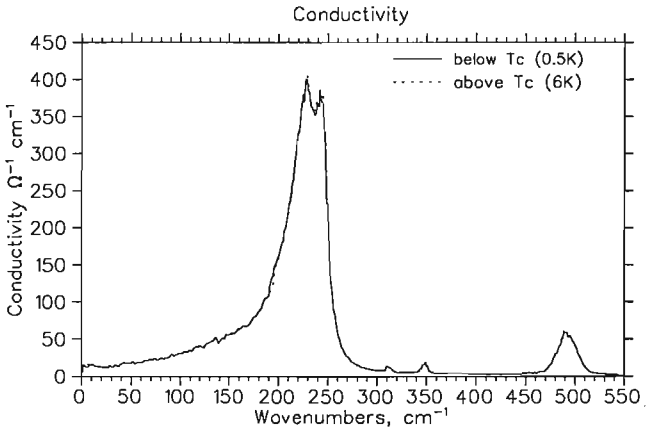

Figure 6.8: Optical Conductivity of $La_{1.875}Ba_{0.125}CuO_4$ at 6K and 0.5K. Figure 6.9 shows a blow up of the low frequency region.

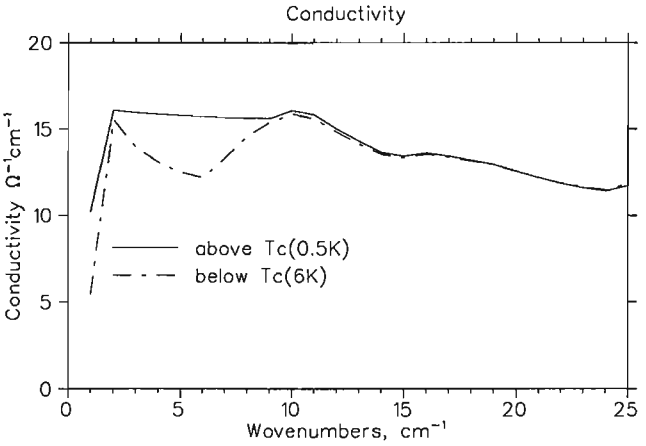

Figure 6.9: Optical Conductivity of $La_{1.875}Ba_{0.125}CuO_4$ at 6K and 0.5K below 25cm^{-1}. The reliability of the data decreases as the frequency decreases and hence the differences in the spectra at the lowest frequencies may be an artifact of the error in the measurements and Kramers-Kronig analysis as opposed to a real difference in the optical conductivity.

gest optical phonons, however the conductivity approaches a non-zero limit (about 15 $\Omega^{-1}cm^{-1}$) and increases slightly below $25cm^{-1}$. Figure 6.9 shows a blow up of the low frequency conductivity. The non-zero limit of the conductivity suggests a non-zero carrier density and charge transport across the c-axis. This charge transport is present above and below the bulk superconducting transition and does not change significantly. This does not support the hypothesis by Young [2] that superconductivity occurs at different temperatures along different crystal axis directions; at 30K along the a-b plane and along the c-axis at 3K, which causes the bulk superconductivity in $La_{1.875}Ba_{0.125}CuO_4$. Instead the carriers in the a-b plane must be responsible for the bulk transition. Because data below $6cm^{-1}$ is generated with a Hagen-Rubens approximation it is possible that reflectance below the transition is different from the reflectance above the transition in this frequency range. The idea that superconductivity occurs at different temperatures along different crystal axis directions should not be discarded until reflectance can be measured at frequencies low enough to detect the plasma edge if it exists. Results from this experiment show that the plasma edge from the bulk superconducting transition in $La_{1.875}Ba_{0.125}CuO_4$, if it exists, is lower in frequency than can be measured by far-infrared spectroscopy.

Chapter 7

Conclusions

7.1 Plasma Edge in $La_{1.875}Ba_{0.125}CuO_4$

Data collected for this thesis suggests that if the plasma edge exists it is below 6cm^{-1}. Thermal reflectance measurements confirm that the reflectance of $La_{1.875}Ba_{0.125}CuO_4$ below the bulk superconducting transition does not differ from the normal state in the 6-250cm^{-1} range.

Absolute reflectance measurements show that the reflectance of $La_{1.875}Ba_{0.125}CuO_4$ drops from 80% at around 250cm^{-1} to a minimum at 100cm^{-1}. This minimum has previously been measured by C. Homes at 50%, but measurements made for this thesis with the Martin-Puplett and Bruker spectrometers indicate that the minimum has a value of 60%. The cause of this difference is unknown and needs to be investigated. It is possible that over time oxygen vacancies in the sample have been filled, slightly changing the properties of the crystal.

Absolute reflectance measurements at low frequency have shown evidence of an increase in reflectance with decreasing frequency in both the normal and superconducting state. A sharp increase in the reflectivity occurs at around 20cm^{-1} to 75% and again at 10cm^{-1} to 90%. Although several measurements corroborate this possible feature, experimental difficulties may have led to the emergence of this feature. It is recommended that the experiment be carried out again with the Martin-Puplett spectrometer or with a time domain measurement to confirm the existence of these

features. This increase in the reflectance at low frequency indicates charge transport. A more detailed study could reveal temperature dependence and help explain the superconducting properties of $La_{1.875}Ba_{0.125}CuO_4$.

Understanding the mechanism of the c-axis transport in the superconducting state may help physicists understand the puzzle of superconductivity in the cuprates. That is, it may help physicists optimize various factors, such as dopant concentration and oxygen deficiency to maximize the superconducting transition temperature. Understanding the factors needed to maximize the superconducting transition temperature will help engineer superconductors for applications and hopefully lead to a room temperature superconductor.

7.2 Low Frequency FTIR

The Bruker spectrometer provides data which is more consistent at high frequencies than the Martin-Puplett spectrometer. In order to increase the range however, the filtering which isolates the He^3 cryostat from the external environment needs to be modified to allow higher frequencies of light to pass through to the sample stage.

The Martin-Puplett spectrometer shows a significantly higher signal to noise ratio over the Bruker for the 6-30cm^{-1} range. The stepper motor in the spectrometer appears to fail at times and may cause a change in the phase. The spectrometer will often lose the position of the zero path which may be a result of the problem with the stepper motor. It may also be a problem with the computer interface. The consistency of the stepper motor in the Martin-Puplett spectrometer will need to be improved in order to achieve accurate reflectance in the lowest possible infrared regions.

Sample measurements from the Martin-Puplett show similar intensity in the power

spectra as those of the reference mirror. This is characteristic for all filtering combinations. Measurements taken with the Bruker indicate a signal size on the sample which is at best 50% lower than the reference mirror. The decrease in sample signal size may be the result of the light from the light pipes entering the He^3 cryostat at an angle which favours the reference path. This indicates it may be possible to improve the performance of the Bruker/He^3 cryostat system.

Using black polyethylene on crystalline quartz as the only filtering in front of the 0.4K bolometer with the Martin-Puplett spectrometer was successful for measuring the 25-125cm^{-1} range. In the future this filtering should be measured with the Bruker spectrometer to compare the intensity of the lamps.

The lowest frequency measurements can be made with the a circular slab of silica borate (or glass) about 2.5 mm in thickness combined with a layer of black polyethylene in front of the bolometer. The black polyethylene may be bonded directly to the glass or it may be bonded to a piece of crystalline quartz.

7.3 Alternative Methods

Terahertz time domain spectroscopy uses high powered monochromatic sources, often from pulsed lasers to probe matter by a "step" method. This means that the source is only emitting one frequency of light while reflectance is being measured. Once the reflectance is measured the source must be adjusted to a different frequency and the reflectance is measured again. This will provide the reflectance measurements in increments or "steps". The high powered sources can produce electromagnetic radiation which is lower in frequency than can be achieved by a mercury arc lamp. The main drawback to this technique is that only one frequency is being produced at any given time, so several experiments must be carried out to gain a picture of the

frequency dependence of the reflectance. Terahertz time domain spectroscopy could be used to look for a plasma edge in the c-axis reflectance of $La_{1.875}Ba_{0.125}CuO_4$ below $6cm^{-1}$. This would overcome the lack of intensity from a mercury arc lamp that limits FTIR to a low frequency cutoff of $6cm^{-1}$.

Appendix A

Reflectance of a Metal

For the model of the relection of light from a solid, consider the model of an electron acting as a damped harmonic oscillator with a driving force of $-eE$, Hooke's law restoring force of $-Kr$ and a frictional damping force proportional to the velocity, $-m\gamma\frac{dr}{dt}$. Applying Newton's second law:

$$m\frac{d^2r}{dt^2} + m\gamma\frac{dr}{dt} + Kr = -eE \tag{A.1}$$

where m is the mass of an electron, K is the force constant of the effective spring, and γ is a frictional constant (ie. the scattering rate).

Assume that the electric field is a harmonic wave with time dependence

$$E = E_0 e^{-iwt}. \tag{A.2}$$

Assuming that the position varies with the same form as the electric field:

$$\frac{dr}{dt} = -iwr_0 e^{-iwt} = -iwr, \tag{A.3}$$

and

$$\frac{d^2r}{dt^2} = (-iw)^2 r_0 e^{-iwt} = -w^2 r. \tag{A.4}$$

Substituting equation A.3 and A.4 into equation A.1 gives

$$-mw^2r - im\gamma wr + Kr = -eE \tag{A.5}$$

then solving for r gives

$$r = \frac{eE}{mw^2 - K + im\gamma w}. \tag{A.6}$$

The polarization equation is given by

$$p = -Ner, \tag{A.7}$$

where N is the dipole per unit volume. Substituting the solutions of r from equation A.6 into equation A.7 gives

$$p = \frac{-Ne^2}{mw^2 - K + im\gamma w}E. \tag{A.8}$$

The electric field in this case is the actual field at the dipole which occurs inside the medium. This can be written as a superposition of the applied field and the fields that arise from the alignment of all other dipoles in the medium. The field from all other dipoles is given as $\frac{p}{3\epsilon_0}$ so that the electric field inside the medium can be written as:

$$E = E_{applied} + \frac{p}{3\epsilon_0} \tag{A.9}$$

where ϵ_0 is the permittivity of free space. Now substituting equation A.9 into equation A.8 and by re-arranging we get

$$p = \frac{\frac{-Ne^2}{m}}{w^2 - \frac{k}{m} + \frac{Ne^2}{3\epsilon_0 m} + iw\gamma} E_{applied} \tag{A.10}$$

Define

$$w_0^2 = \frac{k}{m} - \frac{Ne^2}{3\epsilon_0 m} \tag{A.11}$$

so now

$$p = \frac{\frac{-Ne^2}{m}}{w^2 - w_0^2 + iw\gamma} E_{applied}. \tag{A.12}$$

Maxwell's equations for a metal are as follows:

$$\nabla \cdot E = 0 \tag{A.13}$$

$$\nabla \times E = \frac{-dB}{dt} \tag{A.14}$$

$$\nabla \cdot B = 0 \tag{A.15}$$

$$c^2 \nabla \times B = \frac{dE}{dt} + \frac{1}{\epsilon_0}\frac{dp}{dt} \tag{A.16}$$

For a metal, we can consider the oscillator to have no restoring force, so $w_0 = 0$, therefore,

$$p = \frac{\frac{-Ne^2}{m}}{w^2 + iw\gamma} E_{applied}, \tag{A.17}$$

and taking the derivative we get

$$\frac{dp}{dt} = \frac{\frac{Ne^2}{m} E}{\gamma - iw}. \tag{A.18}$$

From equation A.13 we have the identity:

$$\nabla \times (\nabla \times E) = -\nabla^2 E \tag{A.19}$$

so now

$$\nabla^2 E = \frac{1}{c^2}(\frac{d^2E}{dt^2} + \frac{1}{\epsilon_0}\frac{\frac{Ne^2}{m}}{\gamma - iw}\frac{dE}{dt}) \tag{A.20}$$

Recall that a harmonic wave propagating along the z-axis of the form

$$E = E_0 e^{i(kz - wt)} \tag{A.21}$$

will give

$$\nabla^2 E = -k^2 E, \tag{A.22}$$

$$\frac{dE}{dt} = -iwE \tag{A.23}$$

and

$$\frac{d^2E}{dt^2} = -w^2E. \tag{A.24}$$

Substituting these results into equation A.20 gives

$$-k^2E = \frac{1}{c^2}(-w^2E - \frac{1}{\epsilon_0}\frac{\frac{Ne^2}{m}}{\gamma - iw}iwE) \tag{A.25}$$

and solving for k gives

$$k^2 = \frac{w^2}{c^2} + \frac{iw}{c^2\epsilon_0}(\frac{\frac{Ne^2}{m}}{\gamma - iw}). \tag{A.26}$$

The refractive index is given by:

$$n^2 = (n_1 + in_2)^2 = \frac{c^2}{w^2}k^2 \tag{A.27}$$

and the reflectance can then be calculated,

$$R = \frac{(1-n_1)^2 + n_2^2}{(1+n_1)^2 + n_2^2}. \tag{A.28}$$

Taking Equation A.27 and substituting into Equation A.26

$$n_1^2 + 2n_1n_2i - n_2^2 = 1 + \frac{1}{\epsilon_0}\frac{\frac{Ne^2}{m}}{\gamma^2 + w^2}[\frac{i\gamma}{w} - 1] \tag{A.29}$$

so now,

$$n_1^2 - n_2^2 = 1 - \frac{Ne^2}{m\epsilon_0}\frac{1}{\gamma^2 + w^2} \tag{A.30}$$

and

$$2n_1n_2 = \frac{Ne^2}{m\epsilon_0}\frac{1}{w}\frac{\gamma}{\gamma^2+w^2}. \tag{A.31}$$

The value $\frac{Ne^2}{m\epsilon_0}$ is the square of the plasma frequency, w_p so Equation A.30 and A.31 can both be rewritten as:

$$n_1^2 - n_2^2 = 1 - w_p^2\frac{1}{\gamma^2+w^2} \tag{A.32}$$

and

$$2n_1n_2 = w_p^2\frac{1}{w}\frac{\gamma}{\gamma^2+w^2}. \tag{A.33}$$

Taking Equation A.32 and considering the case where $n_1 \simeq n_2$

$$w_p^2 = \gamma^2 + w^2 \tag{A.34}$$

Typically $w_p \gg \gamma$ so that

$$w_p \simeq w. \tag{A.35}$$

Thus the frequency, w, at which n_1 crosses n_2 gives w_p.

Bibliography

[1] D. Reznik and L. Pintschovius ... Electron-phonon coupling reflecting dynamic charge inhomogeneity in copper oxide superconductors. *NATURE*, 440:04704, 2006.

[2] Young-June Kim, G. D. Gu, T. Gog, and D. Casa. X-ray scattering study of charge density waves in $La_{2-x}Ba_xCuO_4$. *Phys. Rev. B.*, 77:064520, 2008.

[3] A.R. Moodenbaugh, Youwen Xu, and M. Suenaga. Superconducting properties of $La_{2-x}Ba_xCuO_4$. *Phys. Rev. B.*, 38(7):4596–4600, 1988.

[4] R. J. Cava, A. Santoro, Jr. D.W. Johnson, and W. W. Rhodes. Crystal structure of the high-temperature superconductor $La_{1.875}Sr_{0.125}CuO_4$ above and below tc. *Phys. Rev. B.*, 35(13):6716–6720, 1987.

[5] W. Braunisch, N. Knauf, V. Kataev, S. Neuhausen, A. Grutz, A. Kock, B. Roden, D. Khomskii, and D. Wohlleben. Paramagnetic meissner effect in bi high-temperature superconductors. *Phys. Rev. Letters*, 68(12):1908–1911, 1992.

[6] Micheal P. Marder. *Condensed Matter Physics.* John Wiley & Sons Inc., corrected printing edition, 2000.

[7] C.C. Homes, S.V. Dordevic, G.D. Gu, Q. Li, T Valla, and J.M. Tranquada. Charge order, metallic behavior, and superconductivity in $La_{2-x}Ba_xCuO_4$ with x=1/8. *Phys. Rev. Letters*, 96:257002, 2006.

[8] Fredrick Wooten. *Optical Properties of Solids.* Academic Press, 1st edition, 1972.

[9] E. van Heumen and D. van der Marel. *Optical Probes of electron correlations in solids.* arXiv:0807.3261v1 [cond-mat.str-el], 2008.

[10] M. Ortolani, P. Calvani, and S. Lupi. Frequency-dependent thermal response of the charge system and the restricted sum rules of $La_{2-x}Sr_xCuO_4$. *Phys. Rev. Letters*, 94(6):067002, 2005.

[11] K Tamasaku, Y. Nakamura, and S. Uchida. Charge dynamics across the cuo_2 planes in $La_{2-x}Sr_xCuO_4$. *Phys. Rev. Letters*, 69(9):1455–1458, 1992.

[12] T.J. Johnson and G. Zachmann. *Introduction to Step-Scan FTIR.* Bruker.

[13] D.H Martin and E. Puplett. Polarised interferometric spectrometry for the millimetre and submillimetre spectrum. *Infrared Physics*, 10:105–109, 1969.

[14] Peter R. Griffiths and Christopher Homes. *Handbook of Vibrational Spectroscopy.* John Wiley and Sons Ltd., 1st edition, 2002.

[15] M.A. Quijada, D.B. Tanner, F.C Chou, D.C. Johnston, and S.W. Cheong. Optical properties of single-crystal $La_2CuO_{4+\delta}$. *Phys. Rev. B*, 52(21):15485–15403, 1995.